Available online at www.sciencedirect.com
ScienceDirect
Trans. Nonferrous Met. Soc. China 31(2021) 3205−3227
Transactions of Nonferrous Metals Society of China
www.tnmsc.cn

Review of micro-scale and atomic-scale corrosion mechanisms of second phases in aluminum alloys

Yuan-yuan JI[1,2], Yun-ze XU[3], Bin-bin ZHANG[4], Yashar BEHNAMIAN[5], Da-hai XIA[1,2], Wen-bin HU[1,2]

1. Tianjin Key Laboratory of Composite and Functional Materials, Tianjin 300350, China;
2. School of Materials Science and Engineering, Tianjin University, Tianjin 300350, China;
3. School of Naval Architecture and Ocean Engineering, Dalian University of Technology, Dalian 116024, China;
4. CAS Key Laboratory of Marine Environmental Corrosion and Bio-fouling,
Institute of Oceanology, Chinese Academy of Sciences, Qingdao 266071, China;
5. Department of Chemical and Materials Engineering, University of Alberta, Edmonton, Alberta T6G 2V4, Canada

Received 26 August 2021; accepted 27 October 2021

Abstract: Localized corrosion of aluminum (Al) alloys, such as pitting corrosion, intergranular corrosion, and stress corrosion cracking is closely related to the micro-galvanic corrosion between the second phase and the Al matrix. Using high-resolution transmission electron microscopy and first principles calculations, the factors that affect corrosion mechanisms of the second phase in Al alloys at micro-scale and atomic-scale were examined, including the composition and structure of second phase, pH of the environment, stress and adsorption behavior of adsorbates (such as Cl^-, H_2O, OH^- and O^{2-}).

Key words: Al alloys; corrosion; dealloying; first principles calculations

---

1 Introduction

Al is the most abundant metallic element in the Earth's crust, but the low strength of pure Al limits its use in industry [1]. Several other metals can be alloyed with Al to increase its strength [2]. The high specific strength, low density, and good corrosion resistance of Al alloys make them useful in airplanes, ships, and automobiles [2−4]. Commonly used Al alloys with the major alloying elements in them are 2xxx (Cu), 3xxx (Mn), 4xxx (Si), 5xxx (Mg), 6xxx (Mg and Si), and 7xxx (Zn and Mg) [5]. Some second phases, with sizes in micro-scale to nano-scale, are formed inevitably with the addition of alloying elements [6−8]. The elements are added to improve the mechanical properties of Al alloys [9,10], but they can also affect the corrosion of Al alloys due to the formation of the second phase [11,12]. In this sense, except Al phase, any other phases in Al alloy can be called the second phase, intermetallic particles (IMPs) also belong to the second phase.

Pitting is a typical localized corrosion form for Al alloys. The initiation of pitting corrosion in contact with halide ion is attributed to breakdown of passivity, which may obey three possible mechanisms: penetration mechanism, adsorption mechanism and film-breaking mechanism [13], and the second phase is one common site for pitting initiation [14,15]. The distribution of the second phase in the matrix is often heterogeneous. Some second phases will segregate near the grain boundary, causing the electrical potential of the grain boundary to be different from that of the surrounding matrix, and enabling corrosion to

---

Corresponding author: Da-hai XIA, E-mail: dahaixia@tju.edu.cn

DOI: 10.1016/S1003-6326(21)65727-8

spread along the grain boundary [16]. Besides, the second phases are different from the matrix in composition and structure, so their corrosion behavior are also different from the matrix. With the aggregation of hydrogen atoms [17] or the formation of corrosion products, stress is often formed in the second phase or matrix, causing stress corrosion cracking (SCC) of the Al alloy [18] and material failure. The presence of potential difference between the second phase and the matrix will cause micro-galvanic corrosion between them. The potential of the second phase may be higher than the matrix, lower than the matrix, or change during the corrosion process [19,20].

With the development of computer technology, first principles have been widely used in atomic scale simulations [21,22]. The adsorption of various species such as Cl^-, H_2O and O_2 on the surface of Al matrix or the second phases [23−25] and the diffusion of Cl^- in α-Al_2O_3 [26] and α-Cr_2O_3 [27] can be calculated. The adsorption of organic molecules such as deprotonated benzotriazole on the defective metal surfaces (e.g., Cu) can also be calculated [28]. In addition, through first-principles calculations, the surface energy and work function of the matrix and the second phase can be obtained, which can be closely associated with the Volta potential difference (VPD) [29], so as to understand the corrosion behavior of the second phase from the perspective of atoms. High resolution transmission electron microscopy (HRTEM) [30] and quasi in-situ scanning transmission electron microscopy (STEM) [31,32] enabled us to observe corrosion of the second phase of Al alloys at an atomic scale. Here, experiments and first principles were used to explore the corrosion mechanisms of the second phase of Al alloys at an atomic scale. This review discusses several factors that affect the potential difference between the second phase and the matrix: the composition and structure of the second phase, pH and stress, and summarizes the corrosion mechanisms of the second phase in Al alloys in previous researches: dealloying [33] and atomic-scale galvanic cell [34].

2 Corrosion types related to second phase

Besides the pitting corrosion [14], aluminum can undergo intergranular corrosion (IGC) [35], stress corrosion cracking (SCC) [36], and crevice corrosion [37]. These forms of corrosion are believed to be related to the second phase.

2.1 Pitting corrosion

Pitting corrosion is a main corrosion form in Al alloys. A dense passive film forms on the surface of Al in neutral aqueous solutions without corrosive ions. However, when exposed to aggressive anions like Cl^-, Al pitting corrosion is enhanced. Aggressive anions can be transported through a passive film on Al and reach the Al/oxide interface, where they start their specific action (penetration mechanism) [13], or to adsorb on the oxide surface, enhancing the transfer of metal cations from the oxide to the electrolyte (adsorption mechanism) [38]. The film-breaking mechanism requires breaks within the film that give direct access of the anions to the unprotected metal surface [13,39]. Once a pit starts to grow, a cathodic reactant (e.g., O_2) inside the pit is depleted and that shifts most of the cathodic reaction to the exposed surface outside of the pit, while the anodic reaction occurs inside the pit. The anodic reaction products (metal cations) are enriched in the pit and Cl^- migrates into the pit to maintain electrical neutrality. Pit growth is promoted because of the hydrolysis of metal cations, and because the pH in the pit is lower than that outside the pit [13].

Al matrix composites have excellent mechanical properties [40], whereas corrosion often begins at the interface between the Al matrix and the composite particles [41]. AO et al [20] investigated the degradation of a 6063 Al matrix composite containing Si, Cu, Mg, and Fe, and reinforced with TiC and Al_2O_3 particles. They found that the addition of TiC and Al_2O_3 particles refined the grain size and increased the amount of AlMgSiCu and AlSiFe phases at grain boundaries. The surface Volta potential of TiC particles, AlMgSiCu phase and AlSiFe phase was higher than that of Al matrix (Fig. 1), and Al_2O_3 particles did not participate in corrosion because of their insulativity. The authors calculated the surface energy of the low index Miller planes of TiC particles, AlMgSiCu phase, and AlSiFe phase, and chose three planes with the smallest surface energy value to calculate the adsorption energy of a single Cl^-. The results showed that Cl^- could be adsorbed easily on the surface of AlSiFe phase, increasing the concentration of Cl^- and leading to the breakdown of the passive film. That is, AlSiFe phase is the initiation site of the pitting.

Cu−Mn intermetallic particles (IMPs) appeared to have high pitting potential in the corrosion in Al−Cu−Li alloys. LI et al [42] characterized the distribution of elements before and after corrosion using time-of-flight secondary ion mass spectrometry (ToF-SIMS). They found that Cu and Mn were observed in the Al−Cu−Li alloy matrix after pitting corrosion occurred. Due to the enrichment of Cu before corrosion, Al−Cu−Fe−Mn IMPs formed cathode, and the Al matrix was anode; the pitting occurred at the interface of IMPs and matrix (Fig. 2).

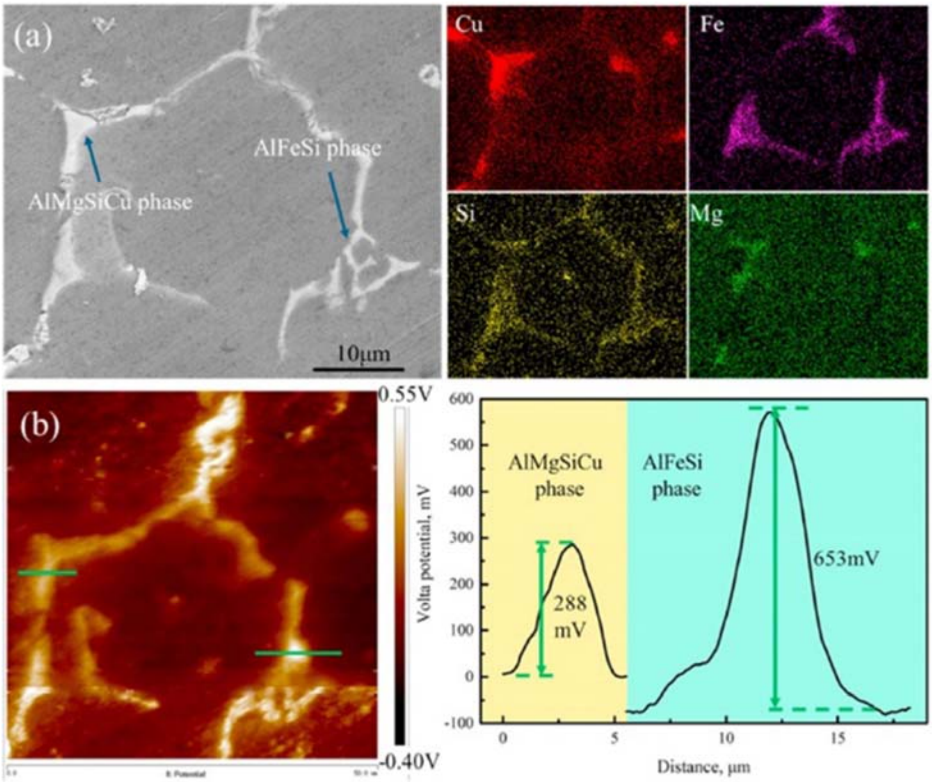

Fig. 1 SEM image and energy dispersive spectroscopy (EDS) results of grain boundaries (a), and Volta potential map and Volta potential profile line (b) of grain boundary of composite [20]

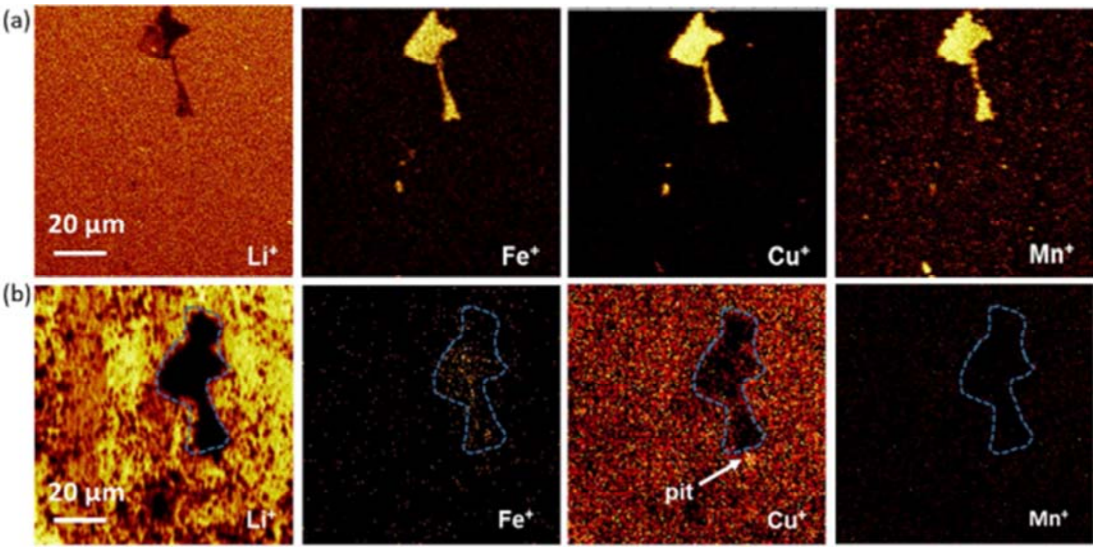

Fig. 2 Positive (Li^+, Fe^+, Cu^+, and Mn^+) ToF-SIMS chemical mapping of AA2050-T8 sample in region of selected Al−Fe−Cu−Mn IMP before corrosion at metallic substrate (a) and after immersion in 0.1 mol/L NaCl for 45 min (b) [42]

Pitting corrosion of Al alloys is affected by the coupling of the second phase with its adjacent metal matrix or other phases. BOAG et al [43] found that the stable pit sites in AA2024-T3 Al alloys often located at the IMPs. The formation of a stable pit in AA2024-T3 Al alloys required three steps: (1) coupling: Al−Cu−Fe−Mn IMPs were coupled with Al_2CuMg (designated as *S* phase) and Al matrix, the former acted as the cathode and they supported the anodic dissolution of *S* phase and Al matrix; (2) dealloying: after dealloying of *S* phase due to corrosion, it became a cathode and Cu redeposited onto nearby Al−Cu−Fe−Mn IMPs, increasing their cathodic activity; (3) pitting: pitting corrosion occurred around the IMPs, increasing the susceptibility of localized corrosion.

The distribution of the second phase is affected by the grain orientation to some extent. MA et al [44] investigated the localized corrosion of AA 2099-T83 Al−Li alloys. They found that the grains with large Schmid factors (the slip plane and the slip direction of a stressed material) experienced more plastic deformation than other grains, increasing the density of the Al_2CuLi phase (designated as T_1 phase) in these grains. Pitting corrosion preferentially occurred in these grains because of the high electrochemical activity of the T_1 phase. As the T_1 phase was preferentially precipitated on {111} Al planes, these sites were more susceptible to corrosion [4].

Pitting in Al alloys is highly related to the number and distribution of the second phase [45]. In the current researches on pitting corrosion of Al alloys, most of them focused on the initiation of pitting. Nevertheless, metastable pit growth and stable pit growth [46] related to the second phase are rarely studied.

2.2 Intergranular corrosion (IGC)

Intergranular corrosion (IGC) usually occurs due to the heterogeneity of the grain boundary and the matrix [47−49]. ZHAO et al [50] investigated the corrosion of a 7A85 Al alloy in an industrial marine atmosphere. They found that deterioration of the mechanical properties of the 7A85 Al alloy was mainly induced by pitting and intergranular corrosion. Figure 3 indicated that grain boundary precipitates were composed of Al, Mg, Zn and Cu, and there were precipitate-free zones (PFZs) (30−60 nm in width) on the sides of the grain boundary [51] which were considered to be Zn, Mg, Cu depletion zones. The potential of PFZs was lower than that of the grain boundary and the matrix before corrosion; corrosion first occurred in the PFZs, and then the IGC pathways formed.

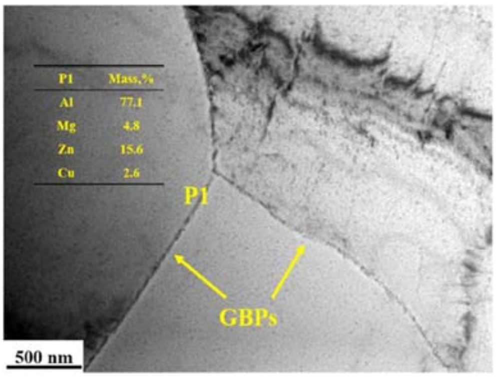

Fig. 3 TEM image of grain boundary precipitates using EDS analysis of precipitates [50]

ZHANG et al [52] studied the influence of trace Cu on the IGC of an AA6082 Al−Mg−Si alloy using high resolution electron microscopy. The AA6082-T6 alloy had very low Cu content (0.06 wt.%), and low angle grain boundaries were almost free of precipitates, indicating a low susceptibility to IGC. However, 13% of the high angle grain boundaries had Al_2Cu precipitates, which accelerated corrosion in the surrounding Al matrix, which acted as the cathode. Selective dissolution of Al also occurred in Al_2Cu, and the remanent Cu enhanced the corrosion of the Al matrix. In addition to Cu, the segregation of other alloying elements at grain boundaries is worth studying. High-throughput computing [5] could be applied to screening elements that might reduce the IGC of Al alloys.

It can be seen that the IGC is mainly related to the precipitation of the second phase at the grain boundary. Heating-aging treatment (HAT) of Al alloys can transform the precipitation phase of the grain boundary from continuous to discontinuous and thus reduce the corrosion rate [53]. A constrained groove pressing (CGP) method can also improve the corrosion resistance of Al alloys by changing the morphology, distribution, and size of the second phase [54].

2.3 Stress corrosion cracking (SCC)

SCC is the degradation of the mechanical properties of a material due to physical stress and a corrosive environment. Out of eight series of Al alloys, 2xxx, 5xxx and 7xxx Al alloys are susceptible to SCC [55]. The SCC in Al alloys involves three mechanisms: (1) anodic dissolution−preferential corrosion occurs along the grain boundary, leading to cracking; (2) hydrogen-induced cracking−corrosion cracks are caused by localized corrosion or concentrated stress; atomic hydrogen is adsorbed at the crack tip, which weakens grain boundaries and causes cracks to form and propagate; (3) passive film ruptures and cracks along the grain boundary [56,57]. Hydrogen embrittlement is one of the main causes of SCC in aluminum alloys [58].

HIRAYAMA et al [59] prepared Al−10Mg alloys that were highly susceptible to SCC that produced various β precipitate (Al_3Mg_2) morphologies. The β precipitate had a tendency to dissolve along the grain boundaries. Pre-existing hydrogen played an important role in the inter-β ligament fracture. The anodic dissolution of the β hardening phase interacting with hydrogen atoms could cause SCC in the Al alloys. However, the experiments were conducted in an Ar gas atmosphere, or in water, in order to reduce the variables, and the influence of other corrosive ions was not considered.

MENG et al [60] found that SCC and IGC resistances of Al−Mg alloys both increased with increasing Zn content. The addition of Zn was beneficial to the formation of $Mg_{32}(Al,Zn)_{49}$ precipitates at grain boundaries, and a transition from precipitation along the grain boundary to homogeneous precipitation in the grain was observed with Zn addition. When the sizes of precipitated particles were larger than 20 nm, they could act as irreversible hydrogen trapping sites [17], and inhibited the formation of hydrogen-induced cracks. Figure 4 shows that the second phase can prevent the formation of hydrogen-induced cracks, changing the corrosion of the alloy from intergranular SCC to pitting corrosion.

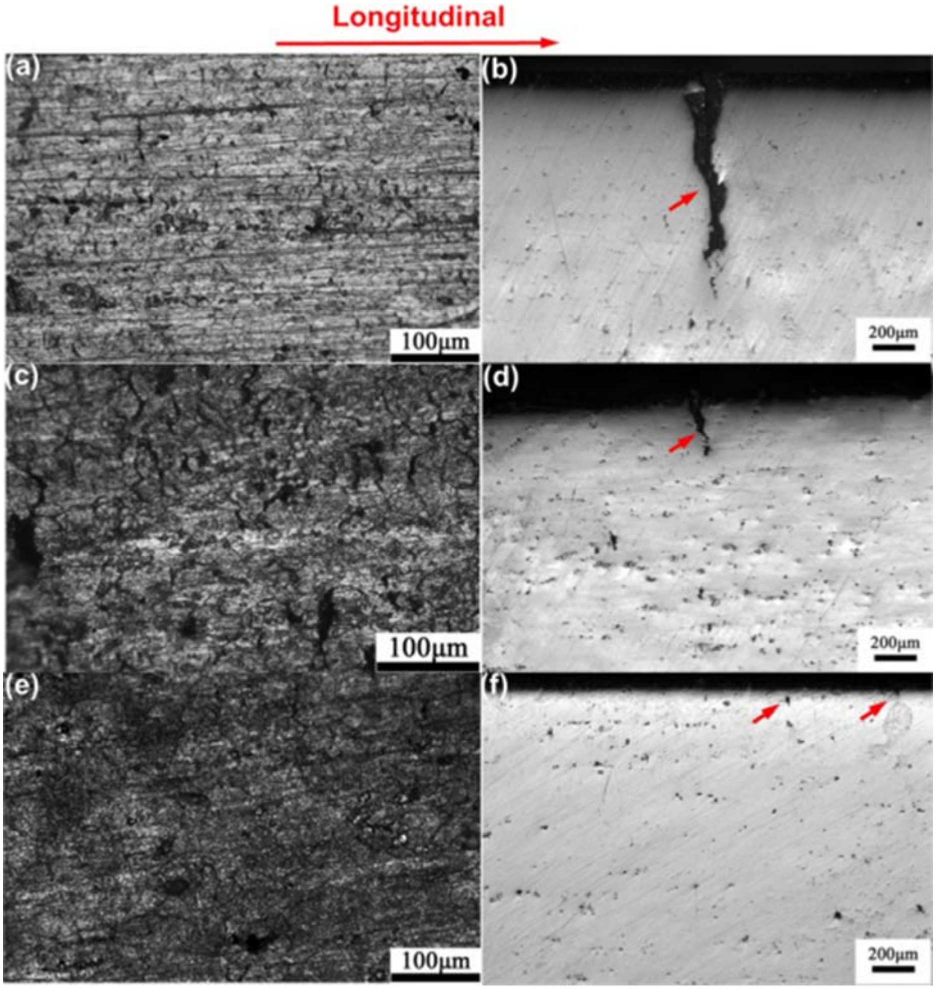

Fig. 4 Optical microscope images of longitudinal section of specimens after slow strain rate testing (SSRT) in acidified NaCl solution for Alloy 1 (a, b), Alloy 2 (c, d), and Alloy 3 (e, f) [60]

The use of first-principles calculations to simulate the trapping of hydrogen by the precipitates would have further confirmed the authors' speculation.

SCC in Al alloys is closely related to the distribution and size of the second phase [61]. Reducing the density of the second phase at grain boundaries can reduce SCC in Al alloys.

3 Main factors affecting corrosion of second phase

According to the different series of Al alloys, a variety of second phases formed in them (Table 1). The Volta potential (VP) is the potential difference between a position infinitely far away from the metal surface and a position just outside the metal surface [74]. Materials with high VP have better corrosion resistance because of their stable electronic states, which means that their valence electrons are restricted to participate in electrochemical reactions [75]. The second phases in Al alloys and the matrix can form local galvanic couples, and the one with lower VP in the couple is easier to be corroded. The difference in the VP between the Al matrix and the second phase determines the tendency of micro-galvanic corrosion: galvanic couples with large VPDs have higher surface reactivity [74], and thus higher corrosion activity. The tendency of a corrosive ion to adsorb on the second phase and the matrix also influences the corrosion process [76]. In the present study, the main factors affecting the VPD between the second phase and the Al matrix were the composition and structure of the second phase, the pH, and the applied stress.

3.1 Composition and structure of second phase

With the different compositions and structures, the VPD between the second phase and the matrix is also different. The second phase containing noble metals such as Cu, Fe, Ag, and Si often appears as the cathode [67,77,78], while the second phase containing elements such as Mg, Zn, and Li often forms the anode [77,79].

ZHU et al [33] characterized the microstructure and the chemical composition of the second phase in AA2070-T8 Al−Cu−Li alloy. They found eleven crystallographic phases and one Guinier-Preston (GP) zone (nanosized coherent pre-precipitates or solute clusters). Among them, seven types of large intermetallic compounds were considered the cathode, which had higher corrosion potential than the surrounding matrix (Fig. 5). The nobility (outstanding resistance to chemical attack, even at high temperatures) of AA2070-T8 increased with the noble element (Cu, Fe) content, and decreased with the Al content. The nobility of these intermetallic particles (IMPs) was closely related to the VPD between the IMPs and the matrix. Although the corrosion potentials of the IMPs in Fig. 5 were obtained by measuring their modeled bulk analogs [33], they were still meaningful because the modeled IMPs contained the target composition and structure.

In addition to directly using scanning Kelvin probe force microscopy (SKPFM) to measure the VPD, the work function can also be used to calculate the VPD between the second phase and the Al matrix:

$$\Delta\Psi=\left|\Psi_{\text{tip}}^{\text{IMPs}}-\Psi_{\text{tip}}^{\text{matrix}}\right|=\left|\frac{\phi_{\text{IMPs}}-\phi_{\text{matrix}}}{e}\right| \tag{1}$$

where $\Delta\Psi$ is the Volta potential of IMPs relative to the Al matrix; $\Psi_{\text{tip}}^{\text{IMPs}}$ and $\Psi_{\text{tip}}^{\text{matrix}}$ are the Volta potentials of the IMPs and the Al matrix, respectively, with respect to the SKPFM tip; ϕ_{IMPs} and ϕ_{matrix} are the work functions of IMPs and the Al matrix, respectively; e is the electron charge [29]. The VPD is directly related to the work function of the metal [1], and the latter can be obtained by first-principles calculations.

Table 1 Main second phases identified in commonly used aluminum alloys

Type of alloy	Typical element	Main second phase	Ref.
2xxx	Al−Cu−Li	$Al_2CuLi(T_1)$, $Al_7Cu_4Li(T_B)$, Al_3Li, $Al_2Cu(\theta)$	[8,62−64]
	Al−Cu−Mg	$Al_2CuMg(S)$, Al_2Cu, AlFeCuMnSi, $Al_{20}Cu_2Mn_3(T)$	[65,66]
5xxx	Al−Mg	$Al_6(Fe,Mn)$, Mg_2Si, Al_3Mg_2	[67]
6xxx	Al−Mg−Si	Mg_2Si, AlFeSi, Al(FeMn)Si, $Al_4Cu_2Mg_8Si_7(Q)$	[68−70]
7xxx	Al−Zn	$MgZn_2$, AlMgCu, Mg_2Si, Al_7Cu_2Fe, Al_2CuMg, $(Al,Cu)_6(FeCu)$	[71−73]

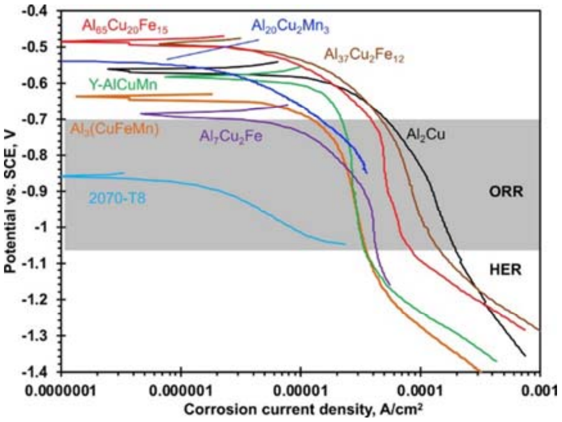

Fig. 5 Cathodic potentiodynamic polarization of surface of seven modeled IMP alloys and AA2070-T8 matrix (The region from the gray zone to the open circuit potential (OCP) of particles indicates the oxygen reduction reaction (ORR) zone [33])

JI et al [80] used first principles to study the effects of the silicon-rich phase and the Mg-containing structure in a corroded Al−Si−Mg alloy fabricated by selective laser melting. Si segregation was caused by the local thermal gradient during laser printing. They found that the work function of pure silicon was higher than that of Al_9Si. They also calculated the work functions of MgSiAl, $MgSi_2Al_2$, and $Mg_2Si_6Al_3$, and found that the addition of Mg could reduce the work function to a certain extent, enabling electron loss from the surface of the alloy.

KONG [81] studied the work functions of the different atomic termination planes of the *S* phase and the T_1 phase in the Al−Cu−Li alloy (Tables 2 and 3). For the *S* phase, first-principles calculations suggested that the work functions of the planes with different terminal atoms were different, mainly due to the arrangement of the atoms on the surface and the influence of the atoms in the sublayer. The planes with the highest Mg content had the lowest work function. The work functions of Planes VII and VIII (Table 2) were higher than that of Plane I because these two planes had less magnesium, and their work functions were mainly determined by Al and Cu. In addition, Mg dissolved first when corrosion began, and Al and Cu became enriched in the *S* phase, as corrosion proceeded.

For the T_1 phase, when the surface contained Li atoms, the work function was relatively small (Table 3) due to the low electronegativity of the Li atom. The work functions of F (Fig. 6(b)) and H (Fig. 6(c)) planes were higher, because the F plane contained only one Li atom, which had little effect on the work function. The Li atoms on the H plane would sink after surface relaxation, and the outer layer contained mainly Al atoms.

Table 2 Work functions of terminations of *S* phase [81]

Plane	Terminal atom	Work function/eV	Mg content/%
(001)-I	Al	4.21	0.00
(001)-II	Cu−Mg	3.65	50.00
(010)-III	Mg	3.44	100.00
(010)-IV	Al−Cu	4.09	0.00
(010)-V	Al−Mg	4.19	33.33
(010)-VI	Al−Cu	4.14	0.00
(100)-VII	Al−Cu−Mg	4.33	25.00
(100)-VIII	Al−Cu−Mg	4.33	25.00

Table 3 Work functions of terminations of T_1 phase [81]

Plane	Terminal atom	Work function/eV
A	Al−Cu−Li	3.64
B	Cu	3.91
C	Al−Cu−Li	3.70
D	Al	4.27
E	Al−Cu−Li	3.89
F	Al−Cu−Li	4.35
G	Al−Cu	4.29
H	Al−Li	4.53
I	Al−Cu	4.12
J	Li	3.40

Lacking direct experimental evidence, such as the observation of the corrosion of different atomic terminal planes in an electrolyte, KONG [81] used calculated work functions to reflect the corrosion resistance of different atomic terminals. It is possible to investigate the corrosion behavior of each atom terminal plane of the second phase by using quasi in-situ STEM, thus we are able to understand the corrosion mechanism of the second phase more deeply from experiments. It is obvious that the second phases with diverse compositions and structures have different terminal atoms. When exposed to the corrosive electrolyte, these atoms have different abilities to confine electrons, which affects the work function of the second phase.

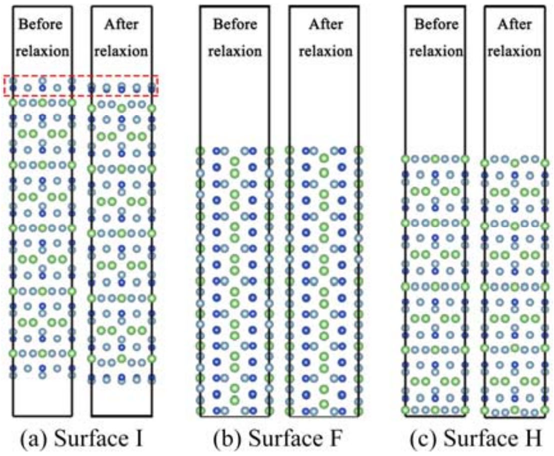

Fig. 6 Atomic configurations of surface I (a), surface F (b), and surface H (c) before and after relaxion (Li atoms are green, Al atoms are light blue, and Cu atoms are dark blue) [81]

3.2 pH

The second phase in Al alloys often exhibit different corrosion patterns at different pH values. Although SKPFM can measure the VPD between the second phase and the Al matrix, it does not measure the kinetics of corrosion. A scanning vibrating electrode technique (SVET) can detect a local corrosion current with good spatial resolution [82]. Because the size of the second phase is extremely small, it is difficult to measure the distribution of galvanic current when it undergoes micro-galvanic corrosion with the matrix by using traditional methods; it is usually studied with synthetic materials with the same element composition with the second phase. In current research, the Mg_2Si phase is generally anodic, and dealloying occurs during the corrosion process [19]. LI et al [82] studied the galvanic corrosion of Al/Mg_2Si in 0.01 mol/L NaCl versus the pH of the solution using a SVET. At pH 2, bulk Mg_2Si actively dissolved, forming the anode, but formed the cathode in alkaline solution. The formation of $Mg(OH)_2$ and MgO on the surface of Mg_2Si pacified the Mg_2Si in alkaline solution.

Using SVET, IKEUBA et al [83] investigated the distribution of galvanic corrosion current of a Q phase ($Al_4Cu_2Mg_8Si_7$)/Al couple at different pH values. They found that the Q phase was cathodic relative to Al at pH 2, 6, and 13, and promoted the anodic dissolution of Al matrix. IKEUBA et al [84] also studied the galvanic corrosion of a $MgZn_2$/Al couple in NaCl solution at different pH values. $MgZn_2$ was anodic relative to Al at pH 2 but cathodic relative to Al at pH 12. $MgZn_2$ underwent dissolution in slightly acidic conditions. At low pH, Mg in the $MgZn_2$/Al couple was preferred to dissolve in NaCl solution. The dissolution of Mg led to the dealloying of $MgZn_2$ and the enrichment of Zn. At pH 12, a stable MgO/$Mg(OH)_2$ passive film was formed on $MgZn_2$. However, the Q phase ($Al_4Cu_2Mg_8Si_7$) was very small and the anode-to-cathode ratio significantly differed from 1:1, so the above results were semi-quantitative [83].

3.3 Stress

LI et al [29] investigated the micro-galvanic corrosion between two primary intermetallic particles−Mg_2Si and α(Al−Fe−Cu) in aluminum alloy AA7075-T6 and Al matrix under the elastic and plastic deformations. The first-principles calculations were used to explain the experimental results. They found the Volta potential differences (VPDs) between Mg_2Si, α(Al−Fe−Cu), and the Al matrix decreased in the elastic stage but increased in the plastic stage (Figs. 7 and 8), and the tensile stress induced no visible change in the particle shape or the morphology of the IMPs.

The experimental phenomenon can be explained by the mechanisms in Fig. 9. Relative to the matrix, the Mg_2Si particle was an anode whereas the α(Al−Fe−Cu) particle was a cathode. Mg_2Si was corroded with the active dissolutions of Mg, and then, Si was enriched at the bottom of the pits. The surrounding Al matrix of α(Al−Fe−Cu) dissolved and the trenches around it are shown in Fig. 9(d). In the elastic deformation stage, the work function of the Al matrix increased because of atomic relaxation, and the work function of Mg_2Si also increased. The calculated VPDs between the second phases and the Al matrix decreased, which is in agreement with the experimental results. In the plastic deformation stage, the concentrations of dislocations within Mg_2Si and α(Al−Fe−Cu) increased, reducing the work functions of Mg_2Si and the Al matrix surrounding the α(Al−Fe−Cu), so the VPDs between the second phases and Al matrix increased.

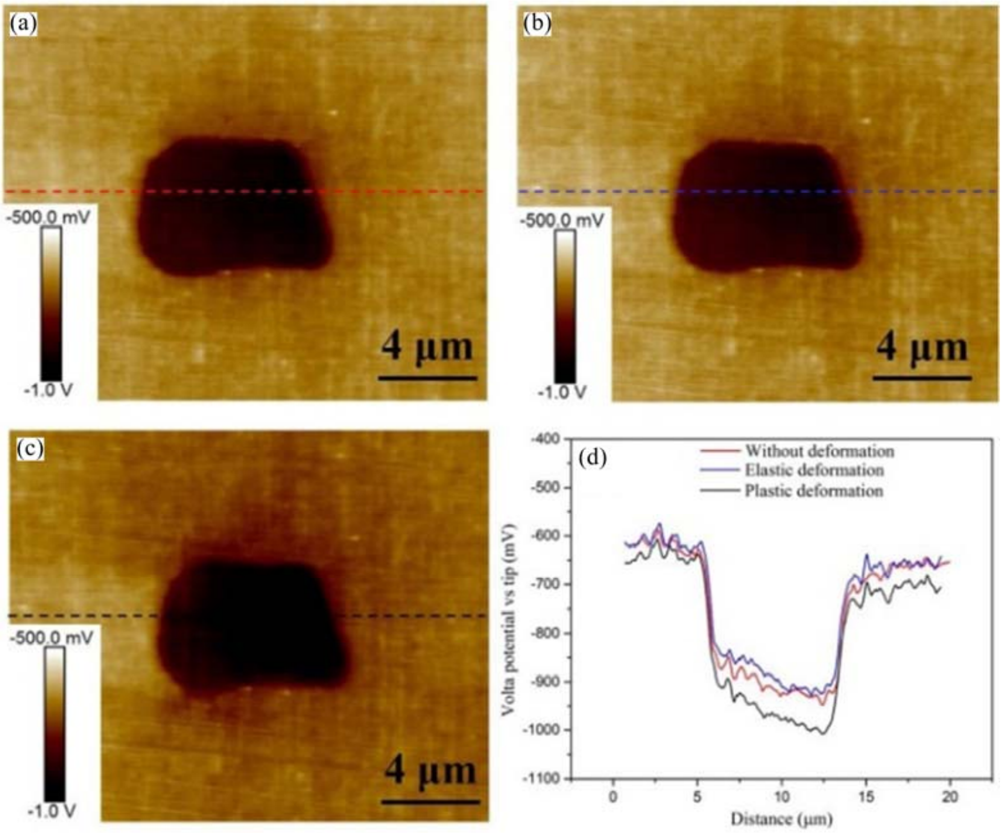

Fig. 7 Volta potentials of Mg_2Si particles in Al matrix under different deformations: (a) Without deformation; (b) Elastic deformation; (c) Plastic deformation; (d) Section of Volta potential [29]

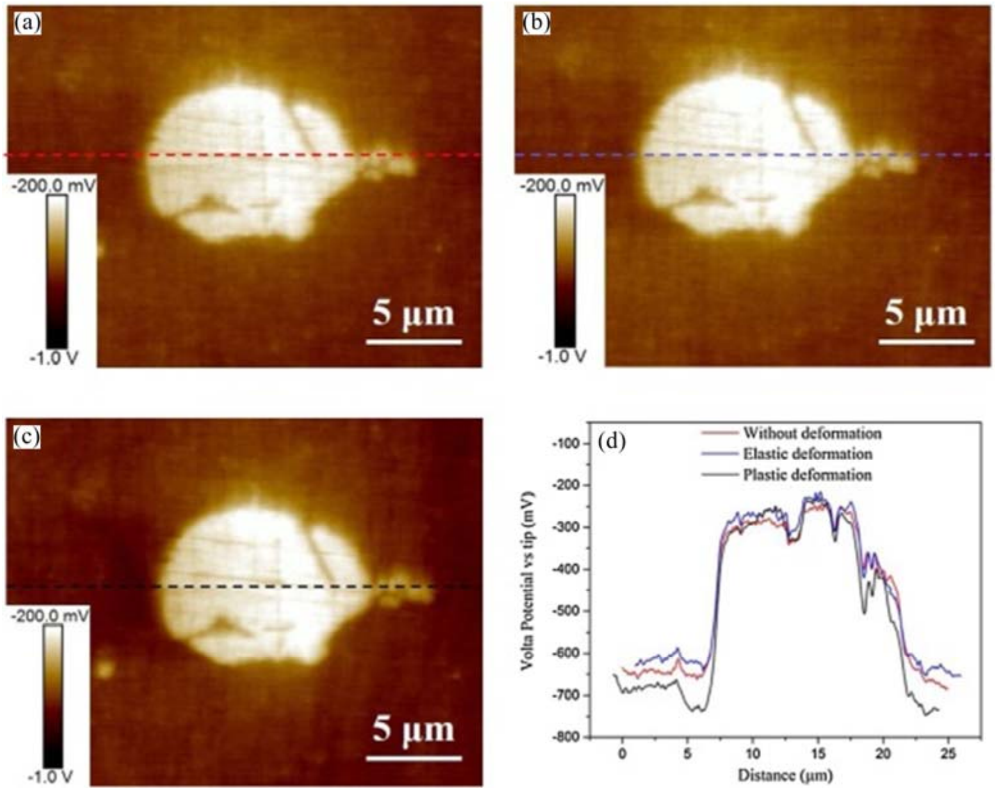

Fig. 8 Volta potentials of α(Al−Fe−Cu) particles in Al matrix under different deformation conditions: (a) Without deformation; (b) Elastic deformation; (c) Plastic deformation; (d) Section of Volta potential [29]

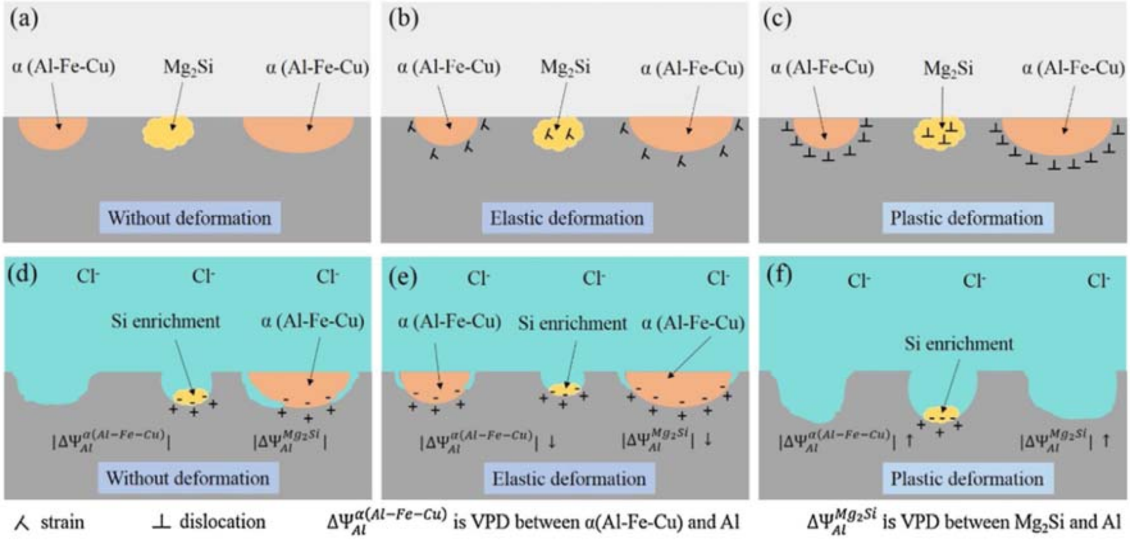

Fig. 9 Schematic of evolution of strain localization and corrosion in aluminum alloy AA7075-T6 under different deformation conditions in 0.1 mol/L NaCl: (a, d) Without deformation; (b, e) Elastic deformation; (c, f) Plastic deformation [29]

KONG et al [85] also studied the work function changes of T_1 phase under tensile stress. They calculated the change of the surface energy and the work function when the tensile strain in the X and Y directions was changed from −2.0% to 2.0% on the 10 planes of the T_1 phase (Table 2, Table 3), and found that changes in the work function were slight. Taking Plane I as an example, the work function of Plane I increased during tensile strain and decreased during compressive strain. The authors believed that the tensile strain caused the distance between the Al atoms on the surface of Plane I and the subsurface layer to decrease (Fig. 6(a)) [81], increasing the electron density and thereby increasing the work function. However, they did not calculate the work function of the aluminum matrix under the same conditions, so the change in the VPD between the T_1 phase and the Al matrix under stress conditions is worth further studying. When studying the effect of tensile stress on the corrosion of the second phase, two main points should be considered: the effect of stress on the work function of the second phase, as well as on the work function of the matrix. Stress mainly affects the arrangement of atoms, which in turn affects the work function of the aluminum alloy. In future, it is necessary to establish a model of the interface between the matrix and the second phase under stress by using the first-principles calculations [86].

3.4 Adsorption

Adsorbates (such as Cl^-, OH^-, H_2O, and O^{2-}) on the surfaces of Al matrix and the second phase behave differently. LI et al [76] investigated the initial growth of passive films on Al_2CuMg and Al matrix. They found that adsorbates such as O^{2-}, OH^-, and H_2O preferred to adsorb on the surface of Al, and the electronic interactions between the adsorbates and Al surfaces were stronger than that between the adsorbates and Al_2CuMg surfaces (Fig. 10 and Fig. 11). The charge transfer from the Al-terminated surface to an adsorbate was larger than that from the Cu, Mg-terminated surface to an adsorbate, because Cu and Mg reduced the charge transfer.

LI et al [76] calculated the adsorption of a single oxygen molecule and a water molecule on the Al and Al_2CuMg surfaces, ignoring the effect of their surface coverage. Adsorbates on the second phase affect its corrosion, and the initial adsorption behavior is affected by the potential difference between the second phase and the matrix. However, once adsorption occurs, the VPDs are associated with the charge on the adsorbates [87]. There are other reasons that affect the adsorption behavior [24,88], which will not be discussed in this review.

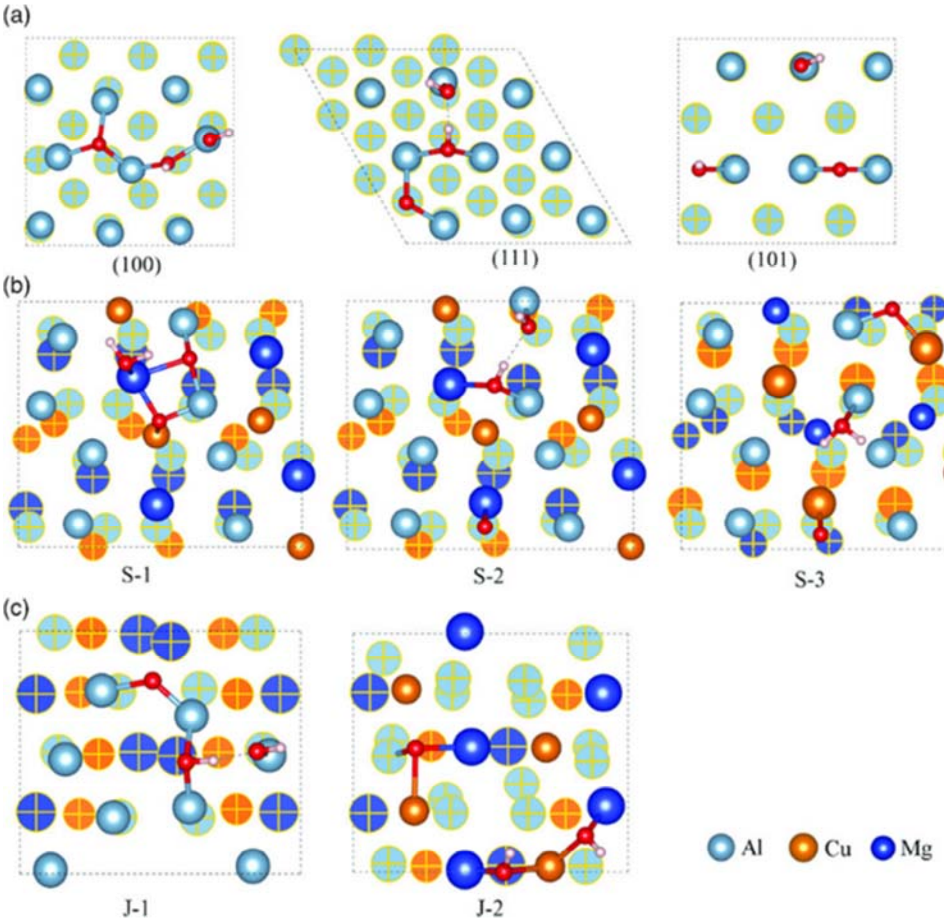

Fig. 10 Top view of co-adsorption of O_2 and H_2O on Al (100), Al (111), and Al (101) (a), Al_2CuMg (101) (b), and Al_2CuMg (001) surfaces (c) [76]

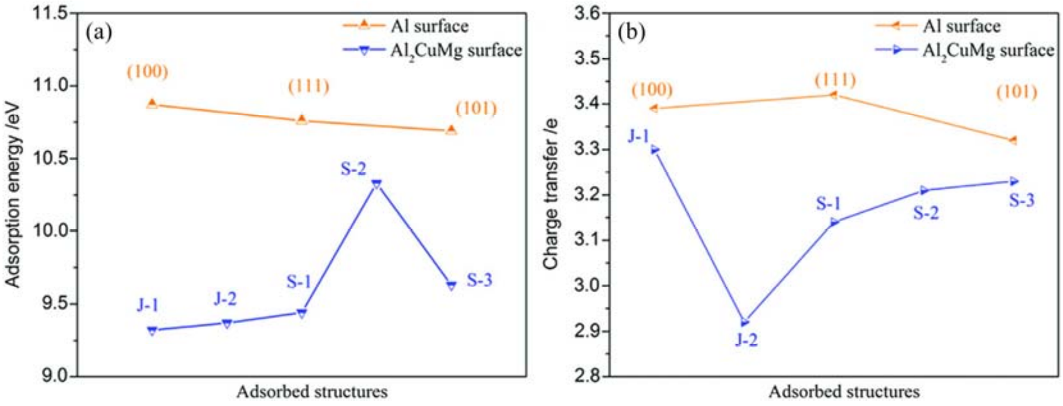

Fig. 11 Adsorption energies (a) and charge transfer (b) of adsorbed structures of dissociative adsorption of O_2 and H_2O on Al (100), Al (111), Al (101), and Al_2CuMg (001) (Surfaces S-1, S-2; Al_2CuMg (101) surfaces: J-1, J-2, J-3) [76]

4 Corrosion mechanisms of second phase

4.1 Dealloying of second phase

In a study of AA2026-T8 Al alloys, ZHU and FRANKEL [89] examined the localized corrosion of Al−Cu−Fe−Mn and *S* phase (Al_2CuMg). Because *S* phase was oxidized during polishing, its Volta potential was higher than that of the surrounding matrix. As the corrosion progressed, Al and Mg in *S* phase were dealloyed, leaving a Cu remnant. As galvanic corrosion occurred between *S* phase and surrounding matrix, continuous trenching formed around, but not beneath *S* phase (Figs. 12 and 13).

However, the dealloying of Al−Cu−Fe−Mn particles only occurred at an early stage of corrosion. Because of the heterogeneity of Al−Cu−Fe−Mn particles, the sites in the Al−Cu−Fe−Mn particle with low Volta potentials were attacked by the 0.1 mol/L NaCl first, and the surrounding matrix was undergoing anodic dissolution at the same time (Fig. 14). A crevice appeared on the bottom of the Al−Cu−Fe−Mn particle (Fig. 15), suggesting that Al−Cu−Fe−Mn particles might have been dissolved and the corrosion product released from the surface into the solution.

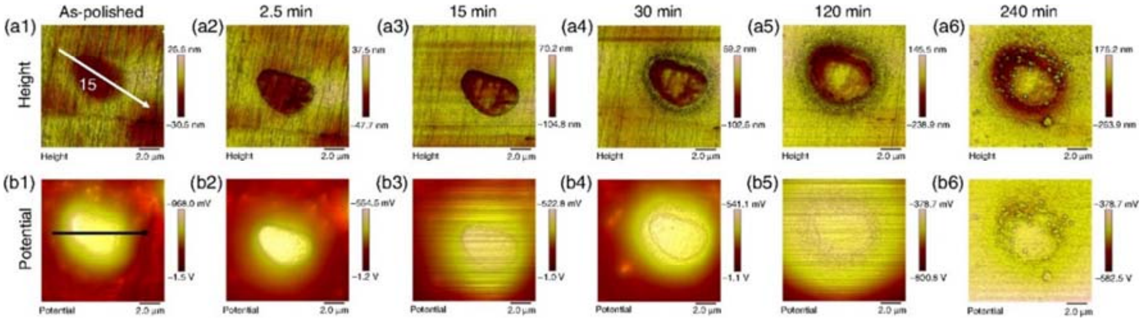

Fig. 12 Topography and Volta potential maps of typical *S*-phase particle in AA2060-T8 after exposure in 0.1 mol/L NaCl for different time: (a1, b1) As-polished; (a2, b2) 2.5 min; (a3, b3) 15 min; (a4, b4) 30 min; (a5, b5) 120 min; (a6, b6) 240 min [89]

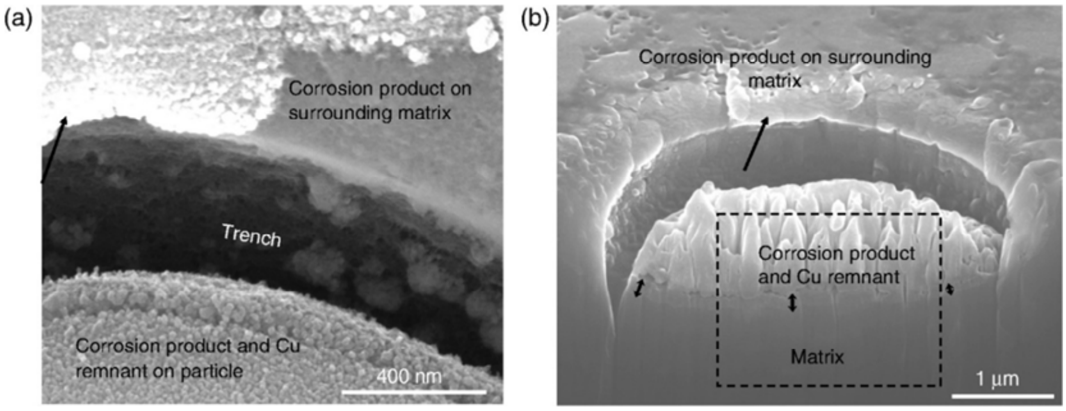

Fig. 13 SEM images of AA2060-T8 alloy after exposure in 0.1 mol/L NaCl for 120 min: (a) Top surface; (b) Cross section of typical *S*-phase particle, matrix, and Cu remanent [89]

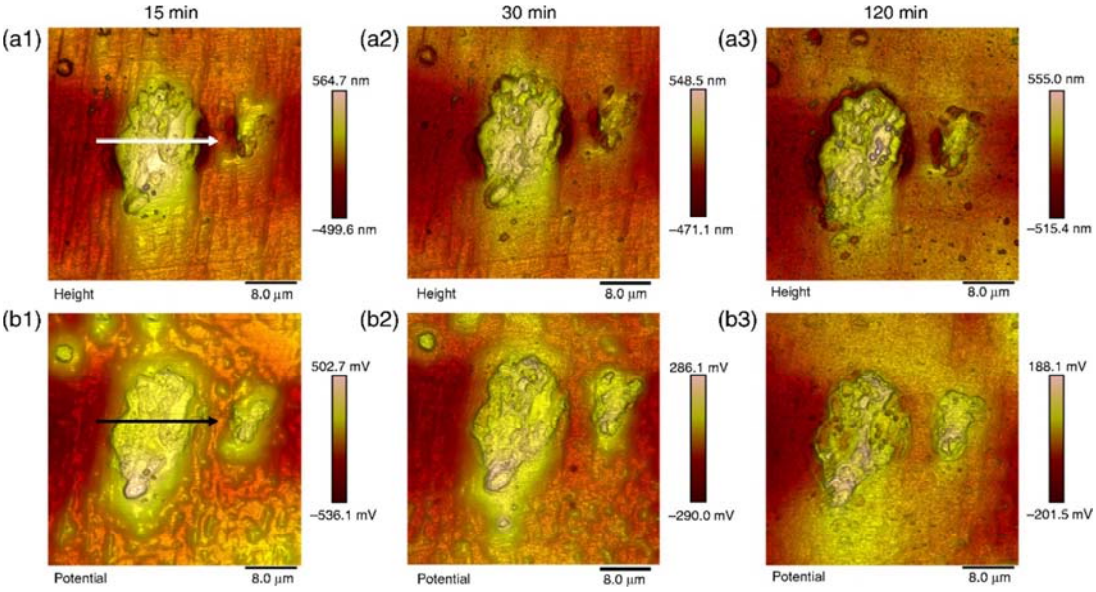

Fig. 14 Topography and Volta potential maps of Al−Cu−Fe−Mn particle in AA2060-T8 after exposure in 0.1 mol/L NaCl for 15 min (a1, b1), 30 min (a2, b2), and 120 min (a3, c3) [89]

ZHU and FRANKEL [89] performed a series of chemical and electrochemical tests on the AA2070-T8 Al alloy immersed in NaCl solution, they studied the preferential dealloying of IMPs, galvanic dissolution of the surrounding matrix, development of trenches, hydrogen evolution at the bottom of trench, and pitting corrosion in alloy matrix [33]. They divided the IMPs/matrix interfacial region into four domains (Fig. 16) [33].

At the interface of the IMPs/electrolyte matrix, which was closed to the top of the trench, the active atoms in IMPs preferentially oxidized, resulting the dealloying corrosion. However, the preferential oxidation of the surrounding matrix was driven by the galvanic interactions between the anodic matrix and the cathodic IMPs. At the bottom of the trench, dealloying also occurred. Cu atoms lost physical support and were released into the electrolyte, redepositing in the surrounding matrix/Cu clusters/electrolyte domain. Redeposited Cu atoms could act as the cathode, driving the oxidation of Al in the surrounding matrix. After dealloying of the IMPs, the redistribution of noble atoms will cause changes in the potential of the surrounding area, and the area where the noble atoms are deposited often acts as a cathode in the ongoing reaction.

Using quasi in-situ STEM and DFT calculations, ZHU et al [32] studied the corrosion of T_B ($Al_{7.5}Cu_4Li$), a nm-scale hardening precipitate in an Al−Cu−Li alloy. They found that the T_B ($Al_{7.5}Cu_4Li$) precipitate was electrochemically nobler than the Al matrix. However, galvanic corrosion preferentially attacked the T_B ($Al_{7.5}Cu_4Li$) precipitate rather than the interface. Localized corrosion of T_B ($Al_{7.5}Cu_4Li$) was initiated by dealloying of Al and Li along T_B ($Al_{7.5}Cu_4Li$) {001} planes because of their low work functions. Cu atoms in T_B($Al_{7.5}Cu_4Li$) lost their physical supports and they were enriched in the Cu (110)//T_B (011)//Al (100) correlation on and around corroded T_B($Al_{7.5}Cu_4Li$) (Fig. 17) because of their diffusion and rearrangements.

ZHU et al [32] calculated the work functions of {001}, {011}, and {111} planes of T_B ($Al_{7.5}Cu_4Li$) (Fig. 18). The results showed that the (001) planes had the lowest work function, which means that corrosion preferentially occurred at {001} planes, consistent with the experimental result.

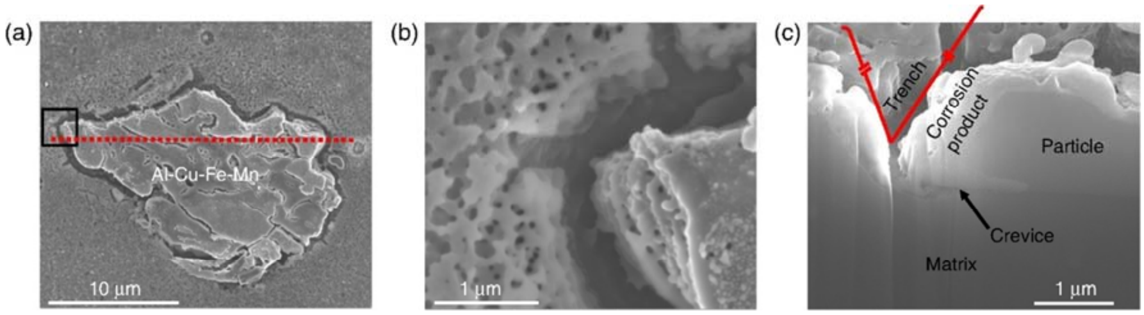

Fig. 15 SEM images of same region in Fig. 14 after corrosion: (a) High-magnification image of Al−Cu−Fe−Mn particle; (b) High-magnification image of black square region in (a); (c) Cross-section region cut by focused ion beam (FIB) along dotted red line in (a) [89]

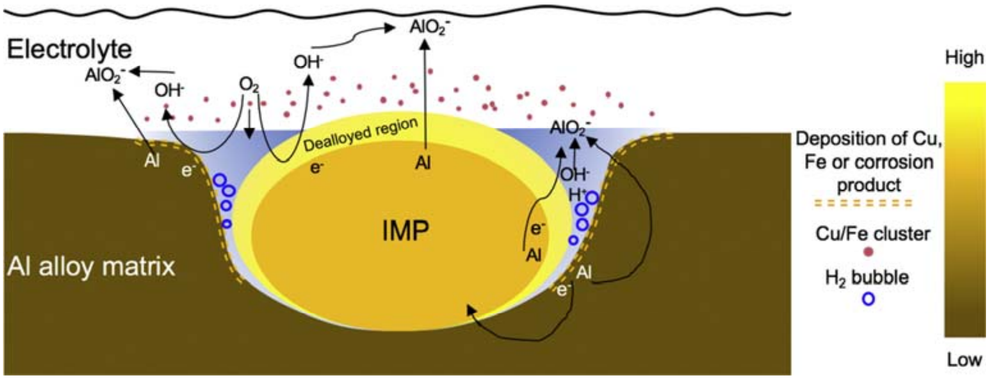

Fig. 16 Schematic illustration of interaction between intermetallic particle (IMP) in alloy and electrolyte (The side bar represents nobility) [33]

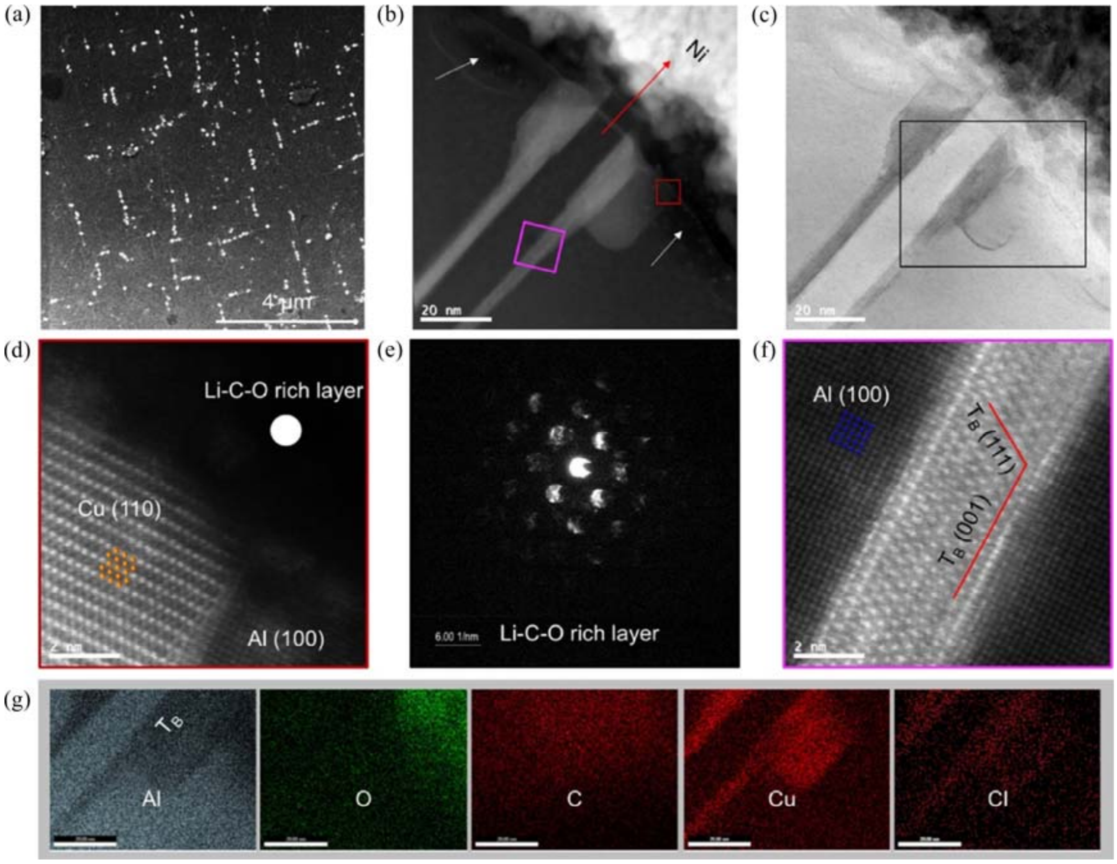

Fig. 17 Surface and cross section analyses of 3 mm Al−3Cu−1.5Li disk sample after corrosion: (a) Back scattered electron (BSE); (b) Dark field (DF); (c) Bright field (BF) STEM image of cross section; (d, f) DF lattice images of corroded structure, corrosion product, Cu sites, and matrix of squared regions in (b); (e) Diffraction pattern of Li−C−O-rich layer in white dotted area in (c); (g) Energy dispersive spectroscopy (EDS) maps of black squared region in (c) (Scale bars in (g) represent 20 nm) [32]

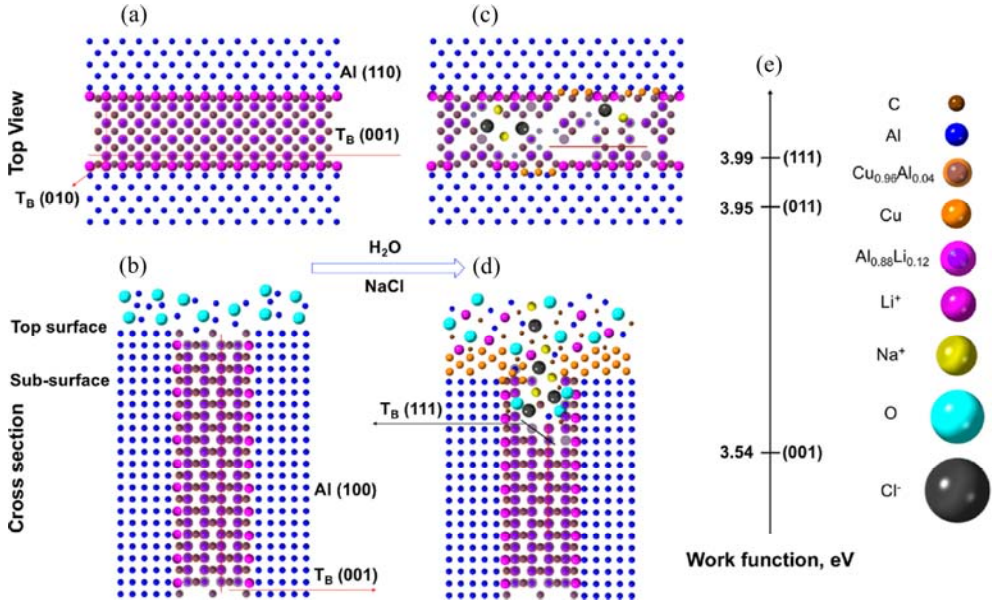

Fig. 18 Schematic representation of mechanism of corrosion processes in specific planes in T_B ($Al_{7.5}Cu_4Li$) and matrix: (a) Top view; (b) Cross section of as-prepared T_B ($Al_{7.5}Cu_4Li$) surface; (c) Top view; (d) Cross section of T_B ($Al_{7.5}Cu_4Li$) surface in Al matrix after electrolyte exposure; (e) DFT calculated work function of (001), (011), and (111) planes, equivalent to {001}, {011}, and {111} planes of T_B ($Al_{7.5}Cu_4Li$) [32]

The work functions and the corrosion resistances of planes with different terminal atoms are usually different. Atoms of active elements are preferentially dissolved, and atoms of noble elements diffuse and rearrange.

4.2 Atomic-scale galvanic cell

There are usually more than one second phase in an Al alloy, they may exist separately or one imbedding in another one. Even for one second phase, its composition and structure are heterogeneous [89]. SUNDE et al [90] described the crystallographic relationships of *T* ($Al_{20}Cu_2Mn_3$) and *S* (Al_2CuMg) phases in Al−Cu−Mg−Ag alloys, they stated that *S* phase could nucleate around or on the *T* phase. That is to say, during the corrosion process, the interior of the second phase may also undergo the micro-galvanic corrosion. ZHANG et al [91−93] observed the atomic-scale galvanic corrosion of *S* phase in 2024 Al−Cu−Mg alloys using high-angle annular dark-field scanning TEM (HAADF-STEM), and they named this type of galvanic corrosion formed by atomic segregation as atomic-scale galvanic cell [34].

WANG et al [92] immersed a 2024 Al−Cu−Mg alloy in 0.5 mol/L NaCl for 15 min, and observed the localized dissolution in the *S* phase (Al_2CuMg) (Fig. 19(c)). Each localized dissolution core corresponded to one nanoparticle embedded in Al_2CuMg (Fig. 19(d)), and localized dissolution

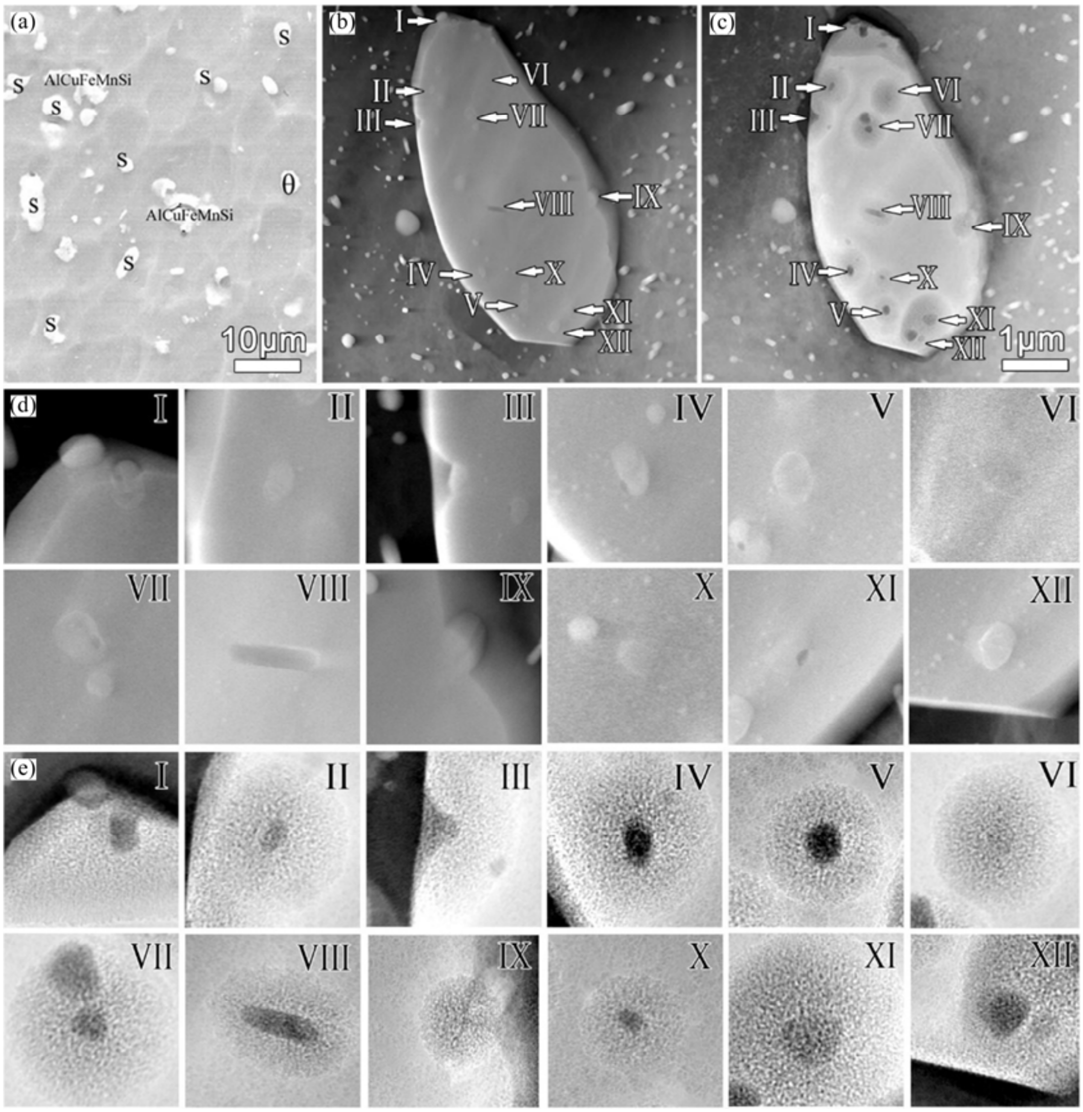

Fig. 19 In situ ex-environmental TEM observation showing local dissolution of *S* phase (Al_2CuMg): (a) SEM image of as-received 2024 Al alloy; (b) HAADF image showing corrosion particle; (c) Particle in (b) after further corrosion; (d) 12 nanoparticles embedded in *S* phase in (b); (e) Zoom-in images showing local dissolution around nanoparticles in (c) [92]

occurred around these nanoparticles (Fig. 19(e)). These particles were not only dispersed in Al_2CuMg, they also appeared in the Al matrix.

The multiple twins in the nanoparticles in Fig. 20(c), can be divided into two types of configuration: parallel shaped twin plates (Fig. 20(c), I and II) and prism shaped twin plates (Fig. 20(c), III and IV) [92]. The two types of twins exhibited different behaviors during corrosion. As shown in Fig. 21, $Al_{20}Cu_2Mn_3$ had multiple twins (prismatic shapes) inside, and the dissolution occurred preferentially in the intersection zone.

In Figs. 22(a) and (b), some $Al_{20}Cu_2Mn_3$ particles (marked with black arrows) dissolved preferentially as well as the Al matrix at the corrosion/Al interface, whereas the $Al_{20}Cu_2Mn_3$ particles labeled I, II, III, and IV did not dissolve. From the zoom-in images of these four particles in Fig. 22(c), it was clear that they contained only parallel twins.

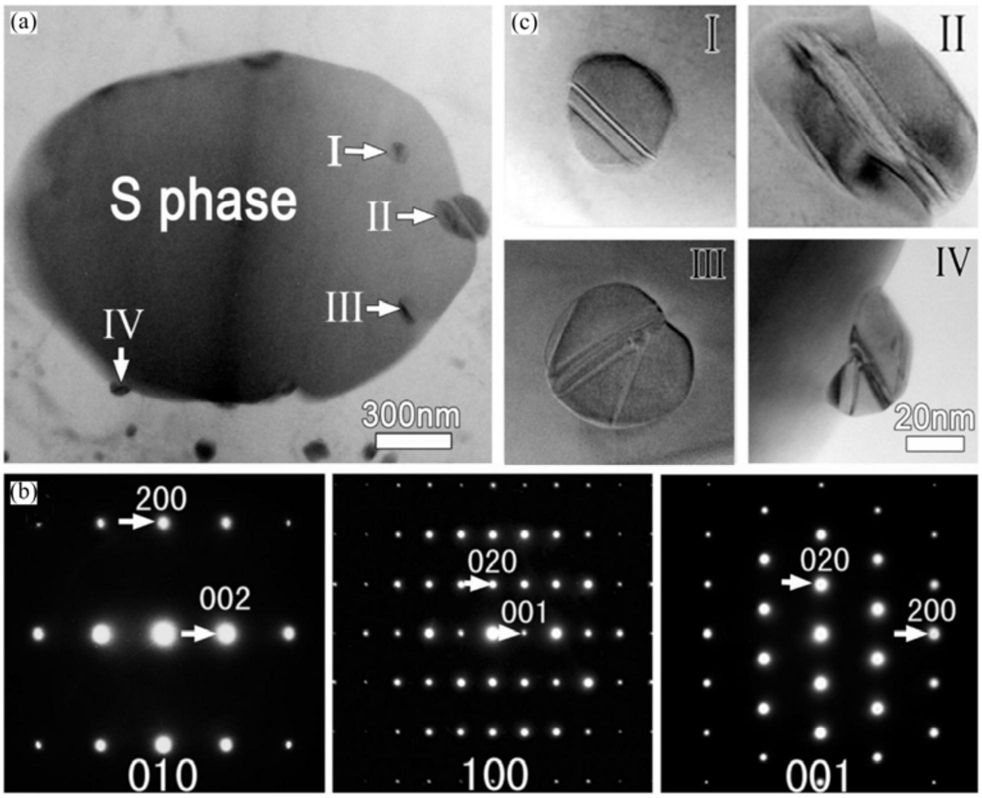

Fig. 20 Bright-field transmission electron microscopy (TEM) image (a) (Arrows point to four nanoparticles embedded in *S* phase), electron diffraction patterns (EDPs) of *S* phase with zone axes of [010], [100] and [001] (b), and zoom-in bright-field TEM images of nanoparticles in (a) labeled as I, II, III, and IV (c) [92]

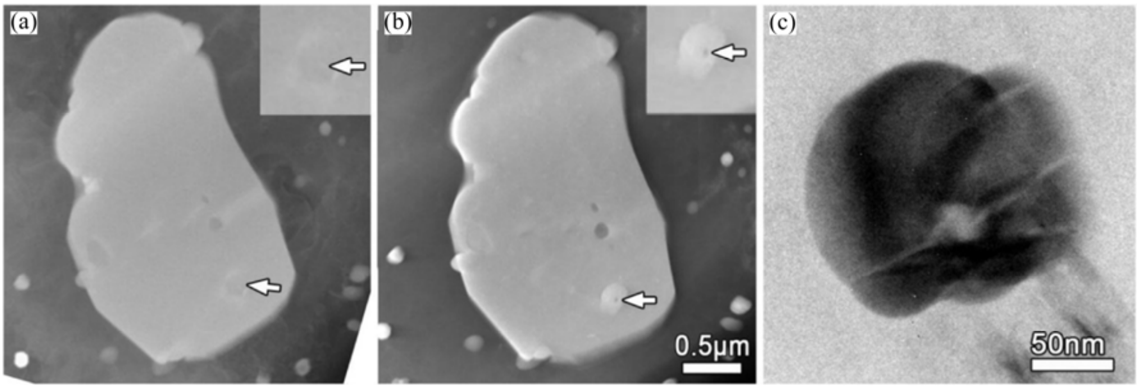

Fig. 21 Observation of initial site where $Al_{20}Cu_2Mn_3$ begins to dissolve: (a) HAADF image showing *S* phase particle embedded with $Al_{20}Cu_2Mn_3$; (b) Particle in (a) suffering immersion in 0.5 mol/L NaCl; (c) Bright-field TEM image of $Al_{20}Cu_2Mn_3$ particles in (a) [92]

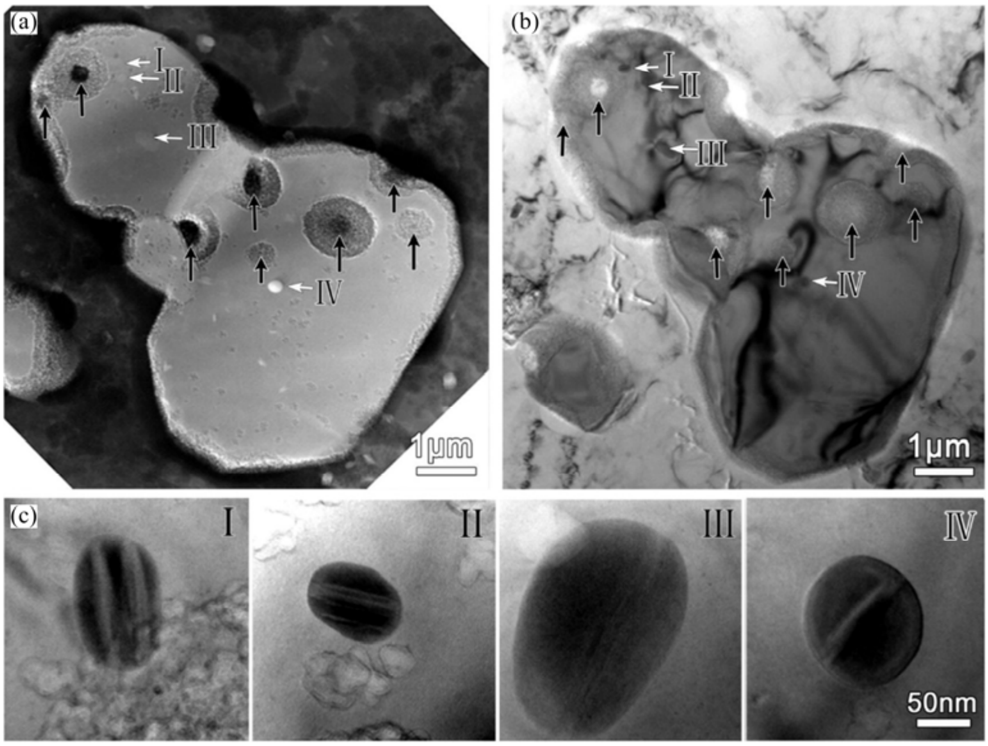

Fig. 22 HAADF image showing *S* phase particle containing dissolved $Al_{20}Cu_2Mn_3$ particles (marked with black arrows) (a), bright-field TEM image (b) corresponding to (a), and zoom-in TEM images of particles I, II, III, and IV (c) [92]

WANG et al [92] found $Al_{20}Cu_2Mn_3$ particles with prismatic twin structures preferentially dissolved in the Al matrix. A curled steak with brighter contrast at a twin boundary in Fig. 23(a) was considered to be sites of Cu enrichment with many defects (Figs. 23(f) and (g)). The darker spots with black arrows in Fig. 23(f) are Al, Cu, Mn depleted zones enriched with O (Figs. 23(b)−(e)). The dealloying of Al and Mn induced the formation of Cu enrichment zones and these Cu-rich zones triggered preferential dissolution of the adjacent zones (Fig. 24), forming atomic-scale galvanic cells [34].

Although the *S* phase serves as the anode of the Al matrix, the dissolution occurs at the interface between the *S* phase and the Al matrix and inside the *S* phase. For the *T* phase, the $Al_{20}Cu_2Mn_3$ matrix and the copper-rich twin boundary form an atomic-scale galvanic cell, consistent with the conclusions by ZHU et al [32].

4.3 Discussion

Pitting corrosion, IGC and SCC of Al alloys are explained by dealloying and atomic-scale galvanic cells, and the impacts of stress, pH and adsorbates on dealloying or the formation of atomic-level galvanic cells are discussed. Figure 25 shows the experiments and simulations related to the corrosion mechanisms of the second phase in Al alloys. Atomic-scale heterogeneous in the second phase triggers an initial dissolution, and the dissolution of the active atoms as well as the redistribution of noble elements in the second phase lead to a formation of more atomic-scale galvanic cells, which complicates corrosion propagation process. For anodic second phases, they serve as pitting locations [94]. For cathodic second phase, pitting initiates within them as a consequence of the dealloying of the active atoms, the redeposition of noble elements accelerates the corrosion process, then trenches are formed at the Al matrix/the second phase interface, finally leading to the undercutting of the second phase [95]. When the second phase particles are distributed at the grain boundaries, the dealloying of the second phase can promote IGC [96].

Stress, pH and adsorbates are the environmental factors affecting the corrosion of the second phase. Stress can change the work function by altering the atoms arrangement. Theoretically, the change of stress will have an impact on both the atomic-scale galvanic cell and dealloying.

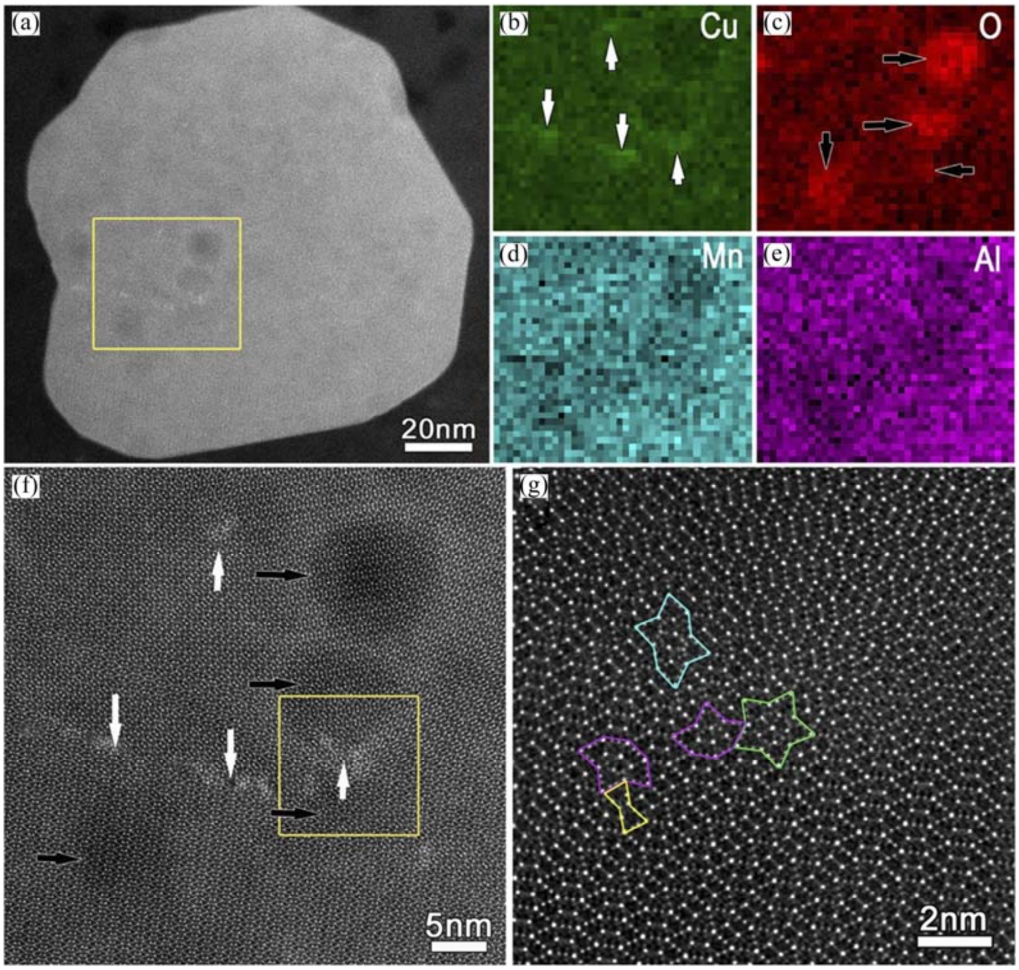

Fig. 23 Heterogeneous chemistry induced local dissolution at atomic scale: (a) HAADF-STEM image showing $Al_{20}Cu_2Mn_3$ particle pre-immersed; (b–e) Electron energy loss spectroscopy (EELS) mapping analysis, focusing on four spots enclosed within box in (a); (f) Magnified image corresponding to boxed area in (a); (g) Magnified image of boxed area in (f), showing a large number of defects within Cu-rich streak [34]

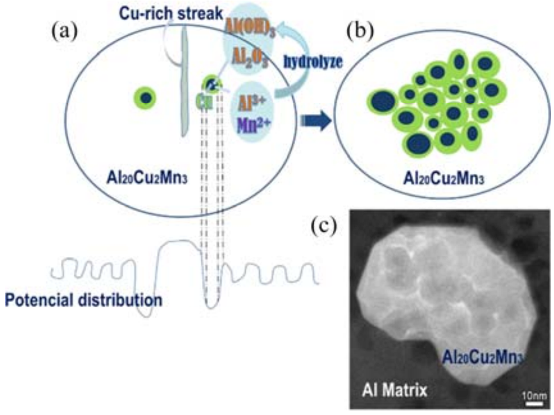

Fig. 24 Propagation of dissolution: (a) Schematic illustration depicting atomic scale dissolution of $Al_{20}Cu_2Mn_3$ as well as formation of Cu-rich rings; (b) Fresh dissolution subsequently propagated over entire surface; (c) HAADF image of dissolved $Al_{20}Cu_2Mn_3$ particle [34]

However, there are limited investigations on in-situ observations of dealloying process of the second phase under stress. The pH can affect the dealloying process significantly. In the electrolyte with low pH, if the remnants of the second phase after dealloying are still active elements, then this second phase will act as the anode (e. g. $MgZn_2$); if the remnants are noble elements, this second phase will serve as the cathode (e. g. *Q* phase). In high pH solutions, the second phase often acts as the cathode because of the formation of the passive film on it. For the adsorbates, their adsorption can change the work functions of the second phase and the Al matrix, which can consequently change the micro-galvanic effect [97]. They can also react with metal cations that formed in dealloying process to form oxides or hydroxides, then prevent the corrosion of the second phase.

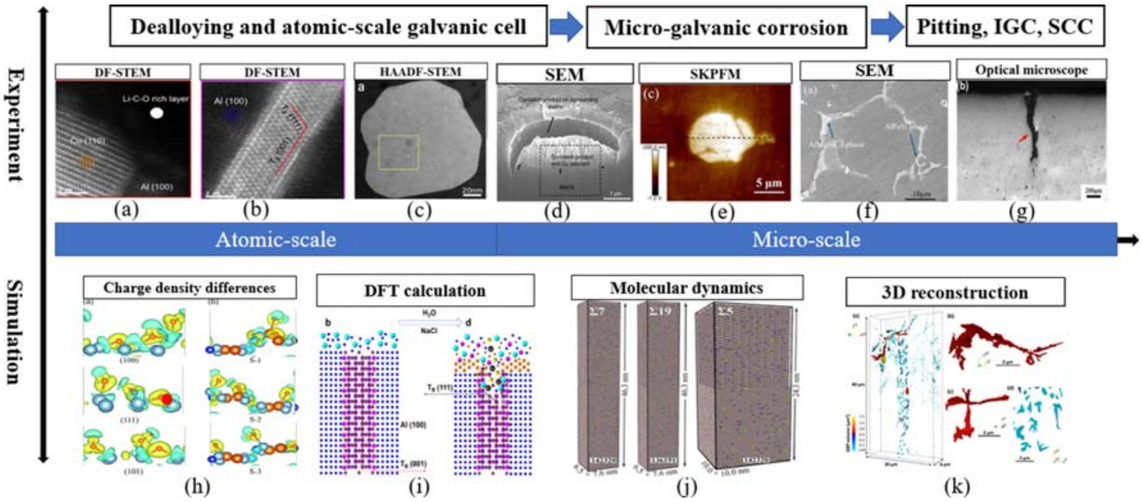

Fig. 25 Corrosion mechanisms in Al alloys at micro- and atomic-scales, including experiments and simulations: (a) Ref. [32]; (b) Ref. [32]; (c) Ref. [34]; (d) Ref. [89]; (e) Ref. [29]; (f) Ref. [20]; (g) Ref. [60]; (h) Ref. [76]; (i) Ref. [32]; (j) Ref. [5]; (k) Ref. [98]

5 Conclusions

(1) The work function, calculated by first principles, reflects the corrosion resistance in different planes and atom terminations of the second phase in Al alloy. In the future, we can analyze the charge distribution of atom terminations to investigate the corrosion mechanisms of the second phase. The effects of environmental conditions on corrosion of the second phase still need to be explored. For example, are the changes in corrosion morphology of Al alloys under different stress states [99] related to charge transfer between the second phase and the matrix, or do they depend on the lattice mismatch between them? First principles can also be used to calculate the impact of ion adsorption on the second phase under stress.

(2) ToF-SIMS, SVET, and in-situ HR-STEM have been successfully applied to observe the second phase corrosion. The development of techniques that can observe features such as atomic rearrangement is needed to further understand the corrosion mechanism.

(3) Alloying elements that improve the corrosion resistance of Al alloys by changing the potential difference between the matrix and the second phase are being investigated by studying the diffusion energy barriers of various alloying elements at grain boundaries [5]. Suitable alloying elements will in future be selected through integrated computation [58], and by controlling the formation, the size, and the distribution of corrosive elements. TAYLOR et al [100−103] established a system that can describe the effects of pH, electrical potential, and Cl^- on the absorption of corrosive ions on the surface of a Ni−22Cr alloy with different alloying elements. This method could be applied to Al alloys.

Acknowledgments

The authors are grateful for the financial support from the National Natural Science Foundation of China (No. 52171077).

References

[1] LIU Min. First-principle calculations of the influences of environmental media and micro-galvanic effect on aluminum localized corrosion [D]. Beijing: University of Science and Technology Beijing. (in Chinese)

[2] IJIRI M, SHIMONISHI D, NAKAGAWA D, YOSHIMURA T. Effect of water jet peening using ultrasonic waves on pure Al and Al−Cu alloy surfaces [J]. International Journal of Lightweight Materials and Manufacture, 2018, 1(4): 246−251.

[3] ABD EL-ATY A, XU Y Z, GUO X, ZHANG S H, MA Y, CHEN D Y. Strengthening mechanisms, deformation behavior, and anisotropic mechanical properties of Al−Li alloys: A review [J]. Journal of Advanced Research, 2018, 10: 49−67.

[4] HUANG Jia-ying, FENG Si-yu, LI Shi-yong, WU Cui-lan, CHEN Jiang-hua. The crystallographic corrosion and its microstructure in an Al−Cu−Li alloy [J]. Journal of Alloys and Compounds, 2021, 861: 158588.

[5] JI Yu-cheng, DONG Chao-fang, CHEN Leng, XIAO Kui, LI

Xiao-gang. High-throughput computing for screening the potential alloying elements of a 7xxx aluminum alloy for increasing the alloy resistance to stress corrosion cracking [J]. Corrosion Science, 2021, 183: 109304.

[6] WANG Shuo, ZHNAG Chi, WANG Jun-sheng. Structures and properties of nano–precipitates in Al−Li alloys [J]. Aeronautical Manufacturing Technology, 2021, 64(9): 68−76, 92.

[7] LI Jin-feng, NING Hong, LIU Dan-yang, ZHENG Zi-qiao. Alloying and micro-alloying in Al−Cu−Li series alloys [J]. The Chinese Journal of Nonferrous Metals, 2021, 31(2): 258−279. (in Chinese)

[8] MA Y, ZHOU X, THOMPSON G E, HASHIMOTO T, THOMSON P, FOWLES M. Distribution of intermetallics in an AA 2099-T8 aluminium alloy extrusion [J]. Materials Chemistry and Physics, 2011, 126(1/2): 46−53.

[9] MATTLI M R, KHAN A, MATLI P R, YUSUF M, ASHRAF A A, SHAKOOR R A, GUPTA M. Effect of Inconel625 particles on the microstructural, mechanical, and thermal properties of Al-Inconel625 composites [J]. Materials Today Communications, 2020, 25: 101564.

[10] YANG Bo-wei, WANG Yu, GAO Min-qiang, GUAN Ren-guo. The response of mechanical property to the microstructure variation of an Al−Mg alloy by adding tin element [J]. Materials Science and Engineering A, 2021, 825: 141901.

[11] KUANG Quan-bo, WANG Ri-chu, PENG Chao-qun, CAI Zhi-yong, FENG Yan, WANG Xiao-feng. Influence of aging treatment on the microstructure, mechanical properties and corrosion behavior of spray deposited Al−Mg−Li−Sc−Zr alloy [J]. Journal of Alloys and Compounds, 2021, 881: 160664.

[12] NIVERTY S, KALE C, SOLANKI K N, CHAWLA N. Multiscale investigation of corrosion damage initiation and propagation in AA7075-T651 alloy using correlative microscopy [J]. Corrosion Science, 2021, 185: 109429.

[13] FRANKEL G S. Pitting corrosion of metals: A review of the critical factors [J]. Journal of The Electrochemical Society, 1998, 145(6): 2186−2198.

[14] BIRBILIS N, ZHU Y M, KAIRY S K, GLENN M A, NIE J F, MORTON A J, GONZALEZ-GARCIA Y, TERRYN H, MOL J M C, HUGHES A E. A closer look at constituent induced localised corrosion in Al−Cu−Mg alloys [J]. Corrosion Science, 2016, 113: 160−171.

[15] MA Y, ZHOU X, HUANG W, THOMPSON G E, ZHANG X, LUO C, SUN Z. Localized corrosion in AA2099-T83 aluminum–lithium alloy: The role of intermetallic particles [J]. Materials Chemistry and Physics, 2015, 161: 201−210.

[16] CHEN Ming-yang, DENG Yun-lai, TANG Jian-guo, FAN Shi-tong, ZHANG Xin-ming. A study of the crystallographic pitting behavior of Al−0.54Mg−0.66Si aluminum alloy in acidic chloride solutions [J]. Materials Characterization, 2019, 148: 259−265.

[17] OGER L, ANDRIEU E, ODEMER G, PEGUET L, BLANC C. Hydrogen-dislocation interactions in a low-copper 7xxx aluminium alloy: About the analysis of interrupted stress corrosion cracking tests [J]. Materials Science and Engineering A, 2020, 790: 139654.

[18] ALI N B, TANGUY D, ESTEVEZ R. Effects of microstructure on hydrogen-induced cracking in aluminum alloys [J]. Scripta Materialia, 2011, 65(3): 210−213.

[19] ZHANG Fan, ÖRNEK C, NILSSON J O, PAN Jin-shan. Anodisation of aluminium alloy AA7075—Influence of intermetallic particles on anodic oxide growth [J]. Corrosion Science, 2020, 164: 108319.

[20] AO Min, LIU Hui-min, DONG Chao-fang, FENG Shan, LIU Jun-cheng. Degradation mechanism of 6063 aluminium matrix composite reinforced with TiC and Al_2O_3 particles [J]. Journal of Alloys and Compounds, 2021, 859: 157838.

[21] HAFNER J. Materials simulations using VASP—A quantum perspective to materials science [J]. Computer Physics Communications, 2007, 177(1/2): 6−13.

[22] HAFNER J. Ab-initio simulations of materials using VASP: Density-functional theory and beyond [J]. Journal of Computational Chemistry, 2008, 29(13): 2044−2078.

[23] XING Hai-rui, HU Ping, LI Shi-lei, ZUO Ye-gai, HAN Jia-yu, HUA Xing-jiang, WANG Kuai-she, YANG Fan, FENG Peng-fa, CHANG Tian. Adsorption and diffusion of oxygen on metal surfaces studied by first-principle study: A review [J]. Journal of Materials Science & Technology, 2021, 62: 180−194.

[24] ZHANG Chuan-hui, CHEN Bao, JIN Ying, SUN Dong-bai. First-principles modeling of layer-defect of Al_2O_3 surface eroded by H_2O and Cl^- [J]. Journal of Physics and Chemistry of Solids, 2017, 110: 129−135.

[25] LIU Min, JIN Ying, ZHANG Chuan-hui, LEYDRAF C, WEN Lei. Density-functional theory investigation of Al pitting corrosion in electrolyte containing chloride ions [J]. Applied Surface Science, 2015, 357: 2028−2038.

[26] LIU Min, JIN Ying, CHEN Bao, LEYGRAF C, WANG Li-ping, PAN Jin-shan. Density functional theory study of influence of oxide thickness and surface alloying on Cl migration within α-Al_2O_3 [J]. Journal of the Electrochemical Society, 2021, 168(8): 081508.

[27] OWARE SARFO K, ISGOR O B, SANTALA M K, TUCKER J D, ÁRNADÓTTIR L. Bulk diffusion of Cl through O vacancies in α-Cr_2O_3: A density functional theory study [J]. Journal of The Electrochemical Society, 2021, 168(7): 071503.

[28] LI Feng-ting, WANG Zhi-kun, JIANG Yun-ying, LI Chun-ling, SUN Shuang-qing, CHEN Shou-gang, HU Song-qing. DFT study on the adsorption of deprotonated benzotriazole on the defective copper surfaces [J]. Corrosion Science, 2021, 186: 109458.

[29] LI Ni, DONG Chao-fang, MAN Cheng, LI Xiao, KONG De-cheng, JI Yu-cheng, AO Min, CAO Jiang-li, YUE Liang, LIU Xiao-teng, DU Min. Insight into the localized strain effect on micro-galvanic corrosion behavior in AA7075-T6 aluminum alloy [J]. Corrosion Science, 2021, 180: 109174.

[30] ZHANG B, WANG J, WU B, GUO X W, WANG Y J, CHEN D, ZHANG Y C, DU K, OGUZIE E E, MA X L. Unmasking chloride attack on the passive film of metals [J]. Nature Communication, 2018, 9(1): 2559.

[31] DUAN S Y, WU C L, GAO Z, CHA L M, FAN T W, CHEN J H. Interfacial structure evolution of the growing composite precipitates in Al−Cu−Li alloys [J]. Acta Materialia, 2017, 129: 352−360.

[32] ZHU Ya-kun, POPLAWSKY J D, LI Si-rui, UNOCIC R R, BLAND L G, TAYLOR C D, LOCKE J S, MARQUIS E A, FRANKEL G S. Localized corrosion at nm-scale hardening precipitates in Al−Cu−Li alloys [J]. Acta Materialia, 2020, 189: 204−213.

[33] ZHU Ya-kun, SUN Kai, GARVES J, BLAND L G, LOCKE J, ALLISON J, FRANKEL G S. Micro- and nano-scale intermetallic phases in AA2070-T8 and their corrosion behavior [J]. Electrochimica Acta, 2019, 319: 634−648.

[34] ZHANG B, WANG J, WU B, OGUZIE E E, LUO K, MA X L. Direct observation of atomic-scale origins of local dissolution in Al−Cu−Mg alloys [J]. Scientific Reports, 2016, 6: 39525.

[35] HUANG Jia-lei, LI Jin-feng, LIU Dan-yang, ZHANG Rui-feng, CHEN Yong-lai, ZHANG Xu-hu, MA Peng-cheng, GUPTA R K, BIRBILIS N. Correlation of intergranular corrosion behaviour with microstructure in Al−Cu−Li alloy [J]. Corrosion Science, 2018, 139: 215−226.

[36] SPEIDEL M O. Stress corrosion cracking of aluminum alloys [J]. Metallurgical Transactions A, 1975, 6(4): 631−651.

[37] PAN Cheng-qun, ZHONG Qing-dong, YANG Jian, CHENG Y F, LI Yu-lin. Investigating crevice corrosion behavior of 6061 Al alloy using wire beam electrode [J]. Journal of Materials Research and Technology, 2021, 14: 93−107.

[38] SOLTIS J. Passivity breakdown, pit initiation and propagation of pits in metallic materials — Review [J]. Corrosion Science, 2015, 90: 5−22.

[39] SZKLARSKA-SMIALOWSKA Z. Pitting corrosion of aluminum [J]. Corrosion Science, 1999, 41(9): 1743−1767.

[40] SINGH J, CHAUHAN A. Overview of wear performance of aluminium matrix composites reinforced with ceramic materials under the influence of controllable variables [J]. Ceramics International, 2016, 42(1): 56−81.

[41] NIE Jin-feng, WANG Fang, CHEN Yu-yao, MAO Qing-zhong, YANG Hua-bing, SONG Zhi-wei, LIU Xiang-fa, ZHAO Yong-hao. Microstructure and corrosion behavior of Al−TiB$_2$/TiC composites processed by hot rolling [J]. Results in Physics, 2019, 14: 102471.

[42] LI Mei-cheng, SEYEUX A, WIAME F, MARCUS P, ŚWIATOWSKA J. Insights on the Al−Cu−Fe−Mn intermetallic particles induced pitting corrosion of Al−Cu−Li alloy [J]. Corrosion Science, 2020, 176: 109040.

[43] BOAG A, TAYLOR R J, MUSTER T H, GOODMAN N, MCCULLOCH D, RYAN C, ROUT B, JAMIESON D, HUGHES A E. Stable pit formation on AA2024-T3 in a NaCl environment [J]. Corrosion Science, 2010, 52(1): 90−103.

[44] MA Y, ZHOU X, LIAO Y, YI Y, WU H, WANG Z, HUANG W. Localised corrosion in AA 2099-T83 aluminium−lithium alloy: The role of grain orientation [J]. Corrosion Science, 2016, 107: 41−48.

[45] ZHAO Kuo, LIU Jian-hua, YU Mei, LI Song-mei. Through-thickness inhomogeneity of precipitate distribution and pitting corrosion behavior of Al−Li alloy thick plate [J]. Transactions of Nonferrous Metals Society of China, 2019, 29(9): 1793−1802.

[46] LI Tian-shu, WU Jun, FRANKEL G S. Localized corrosion: Passive film breakdown vs. pit growth stability, Part VI: Pit dissolution kinetics of different alloys and a model for pitting and repassivation potentials [J]. Corrosion Science, 2021, 182: 109277.

[47] ARTHANARI S, JANG J C, SHIN K S. Corrosion performance of high pressure die-cast Al−6Si−3Ni and Al−6Si−3Ni−2Cu alloys in aqueous NaCl solution [J]. Transactions of Nonferrous Metals Society of China, 2018, 28(11): 2181−2189.

[48] OTT N, YAN Yuan-ming, RAMAMURTHY S, KAIRY S, BIRBILIS N. Auger electron spectroscopy analysis of grain boundary microchemistry in an Al−Cu−Li alloy [J]. Scripta Materialia, 2016, 119: 17−20.

[49] ZHANG R, STEINER M A, AGNEW S R, KAIRY S K, DAVIES C H J, BIRBILIS N. Experiment-based modelling of grain boundary β-phase (Mg$_2$Al$_3$) evolution during sensitisation of aluminium alloy AA5083 [J]. Scientific Reports, 2017, 7: 2961.

[50] ZHAO Qi-yue, GUO Chuang, NIU Ke-ke, ZHAO Jin-bin, HUANG Yun-hua, LI Xiao-gang. Long-term corrosion behavior of the 7A85 aluminum alloy in an industrial-marine atmospheric environment [J]. Journal of Materials Research and Technology, 2021, 12: 1350−1359.

[51] CUI Z Y, LI X G, MAN C, XIAO K, DONG C F, WANG X, LIU Z Y. Corrosion behavior of field-exposed 7A04 aluminum alloy in the Xisha tropical marine atmosphere [J]. Journal of Materials Engineering and Performance, 2015, 24(8): 2885−2897.

[52] ZHANG Xin-xin, LV You, HASHIMOTO T, NILSSON J O, ZHOU Xiao-rong. Intergranular corrosion of AA6082 Al−Mg−Si alloy extrusion: The influence of trace Cu and grain boundary misorientation [J]. Journal of Alloys and Compounds, 2021, 853: 157228.

[53] LIU Xin-yi, ZHANG Di-yao, WANG Chen-chong, WANG Xu, ZHAO Zi-jun, WU Ming, HUANG J C. Effect of grain boundary precipitation on corrosion of heating-aging treated Al−4.47Zn−2.13Mg−1.20Cu alloy [J]. Journal of Materials Research and Technology, 2020, 9(3): 5815−5826.

[54] FAN Ren-jie, ATTARILAR S, SHAMSBORHAN M, EBRAHIMI M, GÖDE C, ÖZKAVAK H V. Enhancing mechanical properties and corrosion performance of AA6063 aluminum alloys through constrained groove pressing technique [J]. Transactions of Nonferrous Metals Society of China, 2020, 30(7): 1790−1802.

[55] RAO A C U, VASU V, GOVINDARAJU M, SRINADH K V S. Stress corrosion cracking behaviour of 7xxx aluminum alloys: A literature review [J]. Transactions of Nonferrous Metals Society of China, 2016, 26(6): 1447−1471.

[56] WANG Jian-jun, ZHA Xiao-qin, ZHENG Guo-hua. Review of the stress corrosion cracking of 7××× series Al alloys [J]. Light Alloy Fabrication Technology, 2020, 48(04): 9−15, 37. (in Chinese)

[57] BURLEIGH T D. The postulated mechanisms for stress corrosion cracking of aluminum alloys: A review of the literature 1980—1989 [J]. Corrosion, 1991, 47(2): 89−98.

[58] DONG Chao-fang, JI Yu-cheng, WEI Xin, XU Ao-ni, CHEN Di-hao, LI Ni, KONG De-cheng, LUO Xie-jing, XIAO Kui, LI Xiao-gang. Integrated computation of corrosion: Modelling, simulation and applications [J]. Corrosion Communications, 2021, 2: 8−23.

[59] HIRAYAMA K, TODA H, FU Dong-sheng, MASUNAGA R, SU Hang, SHIMIZU K, TAKEUCHI A, UESUGI M. Damage micromechanisms of stress corrosion cracking in Al−Mg alloy with high magnesium content [J]. Corrosion Science, 2021, 184: 109343.

[60] MENG Chun-yan, ZHANG Di, ZHUANG Lin-zhong, ZHANG Ji-shan. Correlations between stress corrosion cracking, grain boundary precipitates and Zn content of Al−Mg−Zn alloys [J]. Journal of Alloys and Compounds,

2016, 655: 178−187.

[61] CHEN Song-yi, CHEN Kang-hua, PENG Guo-sheng, LIANG Xin, CHEN Xue-hai. Effect of quenching rate on microstructure and stress corrosion cracking of 7085 aluminum alloy [J]. Transactions of Nonferrous Metals Society of China, 2012, 22(1): 47−52.

[62] ZHANG X, ZHOU X, HASHIMOTO T, LINDSAY J, CIUCA O, LUO C, SUN Z, ZHANG X, TANG Z. The influence of grain structure on the corrosion behaviour of 2A97-T3 Al−Cu−Li alloy [J]. Corrosion Science, 2017, 116: 14−21.

[63] LUO Chen, ALBU S P, ZHOU Xiao-rong, SUN Zhi-hua, ZHANG Xiao-yun, TANG Zhi-hui, THOMPSON G E. Continuous and discontinuous localized corrosion of a 2xxx aluminium–copper–lithium alloy in sodium chloride solution [J]. Journal of Alloys and Compounds, 2016, 658: 61−70.

[64] MA Yan-long, ZHOU Xiao-rong, MENG Xiao-min, HUANG Wei-jiu, LIAO Yi, CHEN Xiao-li, YI Ya-nan, ZHANG Xin-xin, THOMPSON G E. Influence of thermomechanical treatments on localized corrosion susceptibility and propagation mechanism of AA2099 Al−Li alloy [J]. Transactions of Nonferrous Metals Society of China, 2016, 26(6): 1472−1481.

[65] CAO Min, LIU Li, YU Zhong-fen, FAN Lei, LI Ying, WANG Fu-hui. Electrochemical corrosion behavior of 2A02 Al alloy under an accelerated simulation marine atmospheric environment [J]. Journal of Materials Science & Technology, 2019, 35(4): 651−659.

[66] GENG Ji-wei, LI Yu-gang, LIU Gen, XIAO Hong-yu, HONG Tian-ran, HUANG Jie, WANG Ming-liang, CHEN Dong, WANG Hao-wei. Segregation of *S* precipitates at T/Al interfaces and relevant effects on localized corrosion mechanisms in Al−Cu−Mg alloy [J]. Materials Characterization, 2020, 168: 110571.

[67] YASAKAU K A, ZHELUDKEVICH M L, LAMAKA S V, FERREIRA M G S. Role of intermetallic phases in localized corrosion of AA5083 [J]. Electrochimica Acta, 2007, 52(27): 7651−7659.

[68] KUIJPERS N C W, VERMOLEN F J, VUIK C, KOENIS P T G, NILSEN K E, ZWAAG S V D. The dependence of the β-AlFeSi to α-Al(FeMn)Si transformation kinetics in Al−Mg−Si alloys on the alloying elements [J]. Materials Science and Engineering A, 2005, 394(1/2): 9−19.

[69] REMØE M S, MARTHINSEN K, WESTERMANN I, PEDERSEN K, RØYSET J, MARIOARA C. The effect of alloying elements on the ductility of Al−Mg−Si alloys [J]. Materials Science and Engineering A, 2017, 693: 60−72.

[70] ZOU Yun, LIU Qing, JIA Zhi-hong, XING Yuan, DING Li-peng, WANG Xue-li. The intergranular corrosion behavior of 6000-series alloys with different Mg/Si and Cu content [J]. Applied Surface Science, 2017, 405: 489−496.

[71] MENG Qing-jiang, FRANKEL G S. Effect of Cu content on corrosion behavior of 7xxx series aluminum alloys [J]. Journal of the Electrochemical Society, 2004, 151(5): B271−B283.

[72] ANDREATTA F, TERRYN H, de WIT J H W. Effect of solution heat treatment on galvanic coupling between intermetallics and matrix in AA7075-T6 [J]. Corrosion Science, 2003, 45(8): 1733−1746.

[73] JACUMASSO S C, de PAULA MARTINS, de CARVALHO A L M. Analysis of precipitate density of an aluminium alloy by TEM and AFM [J]. REM—International Engineering Journal, 2016, 69(4): 451−457.

[74] ÖRNEK C, ENGELBERG D L. SKPFM measured Volta potential correlated with strain localisation in microstructure to understand corrosion susceptibility of cold-rolled grade 2205 duplex stainless steel [J]. Corrosion Science, 2015, 99: 164−171.

[75] RAHIMI E, RAFSANJANI-ABBASI A, IMANI A, HOSSEINPOUR S, DAVOODI A. Correlation of surface Volta potential with galvanic corrosion initiation sites in solid-state welded Ti−Cu bimetal using AFM-SKPFM [J]. Corrosion Science, 2018, 140: 30−39.

[76] LI Ni, DONG Chao-fang, MAN Chen, YAO Ji-zheng. In situ electrochemical atomic force microscopy and auger electro spectroscopy study on the passive film structure of 2024-T3 aluminum alloy combined with a density functional theory calculation [J]. Advanced Engineering Materials, 2019, 21(12): 1900386.

[77] ZENG Feng-li, WEI Zhong-ling, LI Jin-feng, LI Chao-xing, TAN Xing, ZHANG Zhao, ZHENG Zi-qiao. Corrosion mechanism associated with Mg_2Si and Si particles in Al−Mg−Si alloys [J]. Transactions of Nonferrous Metals Society of China, 2011, 21(12): 2559−2567.

[78] LIEW Yan-han, ÖRNEK C, PAN Jin-shan, THIERRY D, WIJESINGHE S, BLACKWOOD D J. Towards understanding micro-galvanic activities in localised corrosion of AA2099 aluminium alloy [J]. Electrochimica Acta, 2021, 392: 139005.

[79] LI Mei-cheng, SEYEUX A, WIAME F, MARCUS P, ŚWIATOWSKA J. Localized corrosion induced surface modifications of Al−Cu−Li alloy studied by ToF-SIMS 3D imaging [J]. Npj Materials Degradation, 2021, 5: 23.

[80] JI Yu-cheng, DONG Chao-fang, KONG De-cheng, LI Xiao-gang. Design materials based on simulation results of silicon induced segregation at $AlSi_{10}Mg$ interface fabricated by selective laser melting [J]. Journal of Materials Science & Technology, 2020, 46: 145−155.

[81] KONG Min. The corrosion mechanism of intermediate phase in aluminum alloy: First-principles calculations [D]. Guilin: Guilin University of Technology, 2020. (in Chinese)

[82] LI L L, ZHANG B, TIAN B, ZHOU Y, WANG J Q, HAN E H, KE W. SVET study of galvanic corrosion of Al/Mg_2Si couple in aqueous solutions at different pH [J]. Journal of the Electrochemical Society, 2017, 164(6): C240−C249.

[83] IKEUBA A I, ZHANG Bo, WANG Jian-qiu, HAN En-hou, KE Wei. Understanding the galvanic corrosion of the *Q*-phase/Al couple using SVET and SIET [J]. Journal of Materials Science & Technology, 2019, 35(7): 1444−1454.

[84] IKEUBA A I, ZHANG Bo, WANG Jian-qiu, HAN En-han, KE Wei, OKAFOR P C. SVET and SIET study of galvanic corrosion of Al/$MgZn_2$ in aqueous solutions at different pH [J]. Journal of the Electrochemical Society, 2018, 165(3): C180−C194.

[85] KONG Min, WU Jing-Jing, HAN Tian-ru, TANG Xin. Corrosion mechanism of *T*1 phase in Al−Cu−Li alloy: First-principles calculations [J]. Acta Physica Sinica, 2020, 69(2): 027101. (in Chinese)

[86] CHEN Bao, ZHANG Chuan-hui, JIN Ying. First-principles study on surface fracture of Al−Zn−Mg−Cu alloy under stress load and H environment [J]. Surfaces and Interfaces, 2021, 26: 101366.

[87] GUILLAUMIN V, SCHMUTZ P, FRANKEL G S. Characterization of corrosion interfaces by the scanning kelvin probe force microscopy technique [J]. Journal of the Electrochemical Society, 2001, 148(5): B163−B173.

[88] ZHANG Chuan-hui, LIU Min, JIN Ying, SUN Dong-bai. The corrosive influence of chloride ions preference adsorption on α-Al_2O_3 (0001) surface [J]. Applied Surface Science, 2015, 347: 386−391.

[89] ZHU Ya-kun, FRANKEL G S. Effect of major intermetallic particles on localized corrosion of AA2060-T8 [J]. Corrosion, 2019, 75(1): 29−41.

[90] SUNDE J K, JOHNSTONE D N, WENNER S, van HELVOORT A T J, MIDGLEY P A, HOLMESTAD R. Crystallographic relationships of *T*-/*S*-phase aggregates in an Al−Cu−Mg−Ag alloy [J]. Acta Materialia, 2019, 166: 587−596.

[91] ZHANG B, MA X L. A review—Pitting corrosion initiation investigated by TEM [J]. Journal of Materials Science & Technology, 2019, 35(7): 1455−1465.

[92] WANG J, ZHANG B, ZHOU Y T, MA X L. Multiple twins of a decagonal approximant embedded in *S*-Al_2CuMg phase resulting in pitting initiation of a 2024Al alloy [J]. Acta Materialia, 2015, 82: 22−31.

[93] ZHANG Bo, MA Xiu-liang. TEM study on the pitting initiation [J]. Materials China, 2018, 37(11): 866−879. (in Chinese)

[94] KAIRY S K, BIRBILIS N. Clarifying the role of Mg_2Si and Si in localized corrosion of aluminum alloys by quasi in situ transmission electron microscopy [J]. Corrosion, 2020, 76(5): 464−475.

[95] KOSARI A, TICHELAAR F, VISSER P, ZANDBERGEN H, TERRYN H, MOL J M C. Dealloying-driven local corrosion by intermetallic constituent particles and dispersoids in aerospace aluminium alloys [J]. Corrosion Science, 2020, 177: 108947.

[96] PIDAPARTI R M, PATEL R R. Correlation between corrosion pits and stresses in Al alloys [J]. Materials Letters, 2008, 62(30): 4497−4499.

[97] LIU Min, JIN Ying, PAN Jin-shan, LEYGRAF C. Co-adsorption of H_2O, OH, and Cl on aluminum and intermetallic surfaces and its effects on the work function studied by DFT calculations [J]. Molecules, 2019, 24(23): 4284.

[98] GARNER A, EUESDEN R, YAO Yi-chao, ABOURA Y, ZHAO Huan, DONOGHUE J, CURIONI M, GAULT B, SHANTHRAJ P, BARRETT Z, ENGEL C, BURNETT T L, PRANGNELL P B. Multiscale analysis of grain boundary microstructure in high strength 7xxx Al alloys [J]. Acta Materialia, 2021, 202: 190−210.

[99] LI Jin-feng, CHEN Wen-jing, ZHAO Xu-shan, REN Wen-da, ZHENG Zi-qiao. Corrosion behavior of 2195 and 1420 Al−Li alloys in neutral 3.5% NaCl solution under tensile stress [J]. Transactions of Nonferrous Metals Society of China, 2006, 16(5): 1171−1177.

[100] KE Hui-bin, LI Tian-shu, LU Pin, FRANKEL G S, TAYLOR C D. First-principles modeling of the repassivation of corrosion resistant alloys: Part II. Surface adsorption isotherms for alloys and the chloride susceptibility index [J]. Journal of the Electrochemical Society, 2020, 167(11): 111501.

[101] KE Hui-bin, TAYLOR C D. First-principles modeling of the repassivation of corrosion resistant alloys: Part I. O and Cl adsorption energy [J]. Journal of the Electrochemical Society, 2020, 167(11): 111502.

[102] SAMIN A J, TAYLOR C D. First-principles investigation of surface properties and adsorption of oxygen on Ni−22Cr and the role of molybdenum [J]. Corrosion Science, 2018, 134: 103−111.

[103] TAYLOR C D, LI Si-rui, SAMIN A J. Oxidation versus salt-film formation: Competitive adsorption on a series of metals from first-principles [J]. Electrochimica Acta, 2018, 269: 93−101.

铝合金第二相腐蚀机理的微观/原子尺度研究进展

计元元[1,2]，徐云泽[3]，张斌斌[4]，Yashar BEHNAMIAN[5]，夏大海[1,2]，胡文彬[1,2]

1. 天津市材料复合与功能化重点实验室，天津 300350；
2. 天津大学 材料科学与工程学院，天津 300350；
3. 大连理工大学 船舶工程学院，大连 116024；
4. 中国科学院 海洋研究所 海洋环境腐蚀与生物污损重点实验室，青岛 266071
5. Department of Chemical and Materials Engineering, University of Alberta, Edmonton, Alberta T6G 2V4, Canada

摘　要：铝合金的局部腐蚀(如点蚀、晶间腐蚀以及应力腐蚀开裂)与铝基体和第二相之间的微电偶腐蚀密切相关。采用高分辨率透射电子显微镜和第一性原理计算，从微观和原子尺度上分析影响铝合金第二相腐蚀机理的因素，包括第二相的组成与结构、环境的 pH 值、应力以及吸附物质(如 Cl^-，H_2O，OH^-和 O^{2-})的吸附行为。

关键词：铝合金；腐蚀；脱合金化；第一性原理计算

(Edited by Xiang-qun LI)